EUROPEAN ORGANIZATION FOR NUCLEAR RESEARCH

ELASTIC SCATTERING OF 10 GeV/c π^+ AND K^+ MESONS AND OF 9 GeV/c PROTONS ON PROTONS

C. Baglin*), P. Briandet, P. Fleury and G. de Rosny

Ecole polytechnique, Paris, France

P.J. Carlson and K.E. Johansson

University of Stockholm, Sweden

B. d'Almagne, P. Lehmann, F. Richard and D. Treille**)

Lab. de l'Accélérateur linéaire, Orsay, France

Å. Eide†), A. Lundby, A. Navarro-Savoy and L. Staurset††)

CERN, Geneva, Switzerland

V. Gracco

University of Genova and INFN, Genova, Italy

Geneva - 12 May 1975

(Submitted to Nuclear Physics)

---

*) Now at Purdue University, West-Lafayette, Indiana, USA.

**) Also CERN, Geneva, Switzerland.

†) Now at Agder distrikts-högskole, Kristiansand, Norway.

††) Now at University of Oslo, Norway.

ABSTRACT

Angular distributions of π^+p and K^+p elastic scattering have been measured for an incident beam momentum of 10.0 GeV/c. For π^+p elastic scattering almost the complete angular distribution was measured.

The angular distribution of proton-proton elastic scattering was measured for an incident momentum of 9.0 GeV/c in the interval of the four-momentum transfer squared from 0.7 $(GeV/c)^2$ to 5.0 $(GeV/c)^2$.

For π^+p elastic scattering the structures at $-t = 2.8$ $(GeV/c)^2$ and $-t = 4.8$ $(GeV/c)^2$ are less pronounced than at lower momenta. The cross-section for scattering at 90° in the centre-of-mass system is of the order of 1 $\mu b/(GeV/c)^2$.

For K^+p elastic scattering there is a break in the angular distribution around $-t = 3$ $(GeV/c)^2$.

The differential cross-sections for proton-proton elastic scattering decrease smoothly with increasing momentum transfers.

1. INTRODUCTION

Detailed studies of π^-p elastic scattering have been performed for momenta up to 10 GeV/c [1-3]. For π^+p, complete angular distributions exist up to 5 GeV/c [1,2]. Backward scattering has been measured for π^+p up to 17 GeV/c [1,4,5] and for π^-p up to 40 GeV/c [1,6]. Measurements of near forward scattering, i.e. for $-t$ *) < 5 $(GeV/c)^2$, have been reported for π^-p up to 23 GeV/c [7] and for π^+p up to 14 GeV/c [8]. Structures have been observed for $-t$ = 1.2, 2.8, and 4.7 $(GeV/c)^2$. The dip at $-t$ = 2.8 $(GeV/c)^2$ which at 5 GeV/c [2] is equally deep for π^+p and π^-p seems to have developed differently up to 10 GeV/c, where the dip for π^+p is less pronounced.

In the large-angle region a structure was observed for both π^+p and π^-p at $-t$ = 4.7 $(GeV/c)^2$ at 5 GeV/c. A structure at the same t-value is also observed at 10 GeV/c.

For K^+p, forward elastic scattering has been studied up to 200 GeV/c [5,8-13]. The backward peak has been measured around 5 GeV/c [2,11] and at 7 GeV/c [5]. A full angular distribution has been measured at 5 GeV/c as part of our experimental program[2]. Our data at 5 GeV/c indicated a break around $-t$ = 0.9 $(GeV/c)^2$ in the otherwise smoothly decreasing forward K^+p differential cross-section. This break is also present in some high statistics experiments at lower energies[14].

In contrast to πp elastic scattering, the K^+p large-angle scattering shows a smooth behaviour at 5 GeV/c [2].

Proton-proton elastic scattering has been studied in much more detail and also to much higher energies[15-18]. The structure around $-t$ = 1.2 $(GeV/c)^2$ develops in the range 7-10 GeV/c incident proton momentum, where data still are missing. At ISR energies a pronounced dip is seen around $-t$ = 1.4 $(GeV/c)^2$ [17,18].

Recently much attention has been given to models for large-angle scattering involving the interaction between point-like constituents of the elementary particles[19-21]. These models generally predict a fast energy-dependence of the form $s^{-\alpha}$ for fixed c.m. scattering angle. For scattering near 90° in the c.m. system α = 8-12 depending on the elastic reaction. The angular distributions are also predicted for large values of $|t/s|$ and $|u/s|$.

The purpose of this experiment was to measure as complete an angular distribution as possible for π^+p and K^+p elastic scattering at 10 GeV/c. This is a part of our experimental program involving complete measurements at 5 GeV/c

---

*) Throughout this paper, s, t, and u designate the three Mandelstam variables, where for the reaction m + p → m + p, s is the square of the centre-of-mass energy, t is the four-momentum transfer squared between incident and outgoing m, and u is the four-momentum transfer squared between incident m and outgoing proton p.

[already published[2)]], measurements of positively charged particles at 10 GeV/c (this experiment), and measurements at 6.2 GeV/c involving negatively charged incident particles[22)].

In addition, during a small run, data on proton-proton elastic scattering at 9 GeV/c were collected.

The results of the π^+p and K^+p data at 10 GeV/c have partly been reported earlier[23,24)]. This paper presents some details of the experimental apparatus and of the data acquisition system (Sections 2 and 3), a detailed discussion of the data analysis (Section 4), and finally the experimental results are presented and discussed (Section 5).

2. EXPERIMENTAL SET-UP

2.1 General design

The experiment was designed to study differential cross-sections over the complete t-range. Both for π^+p and K^+p elastic scattering the differential cross-sections extend over six orders of magnitude. Taking this into account, the experimental apparatus must have a good capability of detecting high event-rates, and also a high resolution in order to be able to select the relatively rare large-angle elastic events from topologically similar inelastic events.

A high event rate was obtained by having a high intensity incident beam, a long hydrogen target, and a large angular acceptance. In order to favour the large-angle scattering where the cross-sections were low, special trigger conditions were introduced in order to suppress the forward peak of π^+p scattering. The use of wire spark chambers to detect the trajectories gave high spatial resolution, and magnetic analysis to measure the momentum of one of the outgoing particles gave high background rejection.

The experimental set-up shown in Fig. 1 was of a classical spectrometer type. The object was to measure the trajectories of the incident particle and the two scattered particles, and to momentum-analyse one scattered particle whenever it was possible. The incident beam was defined by four scintillation counters: S_1, S_2, S_3, and S_4. Four hodoscopes served to determine the incident trajectory. The Čerenkov counters C_1, C_2, and C_3 specified the signature of the incident particle. The scattered particles were detected by the trigger counter telescopes T_1, T_2, T_3, and T_4, and the outgoing trajectories were registered by the respective wire spark chamber telescopes W_1, W_2, W_3, and W_4. The veto counter V_1 placed in front of the target served to limit the beam spread, and the veto counter V_2 placed downstream of the target detected non-interacting particles. The spectrometer magnet M had a gap of $100 \times 100 \times 50$ cm^3 and an integral $\int B\, d\ell$ of around 1.5 Tm. The Čerenkov counter C was filled with freon at atmospheric pressure and detected pions scattered in the forward region.

2.2 Incident beam

The unseparated incident beam contained 78% p, 20.6% π^+ and μ^+ and 1.4% K^+ when the PS was run with 21 GeV/c protons. Figure 2 shows the layout of the beam. With a momentum spread of 1% the intensity was typically 7×10^5 particles per burst of 400 msec duration.

The trajectory of the incident particle was determined by four hodoscope counters, each hodoscope being composed of a number of 3-5 mm wide "finger" scintillators. The hodoscopes were arranged in pairs of two with the scintillator elements making an angle of 90°. The scintillation counters S_1 - S_4, which were large enough to cover the extension of the beam, were used to count the number of incoming particles. A coincidence between these four counters was required for the incoming particle to be counted. The signature of the incident particle was given by three threshold Čerenkov counters, which were filled with hydrogen. The threshold pressure to detect pions is 0.7 atm and to detect kaons 9 atm. Figure 3 shows the pressure curve for C_2. The working pressure was chosen to be 7 atm which is well below the pressure at which kaons were counted. The pressure curve for C_1 and C_3 is shown in Fig. 4, from which the working pressure for C_1 and C_3 was chosen to be 11.6 atm. From Fig. 4 the contamination in the kaon sample is estimated to be 0.3%.

2.3 Counter telescopes and anticounters

The scattered particles were detected by four scintillator-telescopes T_1 - T_4 (Fig. 1). Each telescope consisted of two layers of scintillators, one horizontal and one vertical. The horizontal counters were large and arranged in such a way as to give information on whether the particle had passed through the upper or lower part of the telescope. The vertical counters being smaller gave a better determination of where the particle had passed. Table 1 gives the sizes of the telescopes.

The counter telescopes served to form the trigger for the experiment (see Section 2.4). The division of the telescopes into smaller elements made it possible to select fairly coplanar events and to distinguish between forward, large-angle, and backward events.

The angular regions around the target, which were not covered by the counter telescopes or the beam hodoscopes were covered by a set of anticounters. The reason was to sort out clearly inelastic events already on the level of the trigger formation.

2.4 Logic

An incident particle was defined by a coincidence between the four beam counters. The hole counter V_1 in front of the target was used in anticoincidence

in order to remove the halo of the beam and so get a better definition of the beam. The counter V_2 situated downstream of the target was used in anticoincidence to remove the particles going through the target without interacting. Symbolically then the sixfold coincidence $S_1 \cdot S_2 \cdot S_3 \cdot S_4 \cdot \bar{V}_1 \cdot \bar{V}_2$ *) defined an incident particle of any kind interacting in the target.

The Čerenkov counters in the beam defined the signature of the incident particle. The pion signature was given by a signal in C_2 together with a signal in C_1 or C_3, the kaon signature was given by a coincidence between C_1 and C_3 and no signal in C_2, and the proton signature was given when no signal in any of the counters was present. This is summarized in symbolic form in Table 2.

For the scattered particles certain combinations of the trigger counters were required in order to get a more selective triggering on elastic events. One and only one particle was required within each telescope, and a rough test of the coplanarity was done by requiring an up-down symmetry of trigger counters situated on different sides of the incident beam.

An additional requirement that was introduced on the trigger level was the suppression of forward-scattered pion events. This was done in order to favour more rare events such as large-angle and backward scattering. The T_3 telescope was divided into a left and a right section, where the left section was composed of the three vertical counters closest to the beam and so covered the small angular region where forward-going pions were not allowed.

The main event trigger was constructed by eight different counter combinations**):

$$E_1 : T_1(\text{down}) \cdot T_3(\text{right, up})$$
$$E_2 : T_1(\text{up}) \cdot T_3(\text{right, down})$$
$$E_3 : T_1(\text{down}) \cdot T_3(\text{left, up}) \cdot \bar{\pi}$$
$$E_4 : T_1(\text{up}) \cdot T_3(\text{left, down}) \cdot \bar{\pi}$$
$$E_5 : T_2(\text{down}) \cdot T_4(\text{up}) \cdot \overline{T_1}$$
$$E_6 : T_2(\text{up}) \cdot T_4(\text{down}) \cdot \overline{T_1}$$
$$E_7 : T_1(\text{down}) \cdot T_3(\text{left, up}) \cdot \pi \cdot \bar{C}$$
$$E_8 : T_1(\text{up}) \cdot T_3(\text{left, down}) \cdot \pi \cdot \bar{C} .$$

E_1 and E_2 covered the regions $1.5 < -t < 6$ $(\text{GeV/c})^2$ and $1.5 < -u < 6$ $(\text{GeV/c})^2$; E_3 and E_4 gave forward and backward K^+p elastic scattering, and for part of the

---

*) Throughout this paper the symbols used in this context have the following meanings, which are closely connected to the electronic units used in the experiment: the dot indicates a coincidence, the plus indicates an OR, the bar indicates an antisignal.

**) The notation π stands for incident pion, $\bar{\pi}$ stands for veto of incident pion, $\bar{C}$ stands for veto of Čerenkov counter C (Fig. 1).

run also pp elastic scattering; E_5 and E_6 covered the large angles (part of the events produced here had no magnetic analysis); E_7 and E_8 finally gave backward elastically scattered pions.

For the main run these triggers were combined with an incident pion or kaon. The over-all trigger rate was typically around 10 per burst when the forward pions were excluded. The event signals E_1- E_8 initiated the following processes:

i) switched voltage on the spark chambers;

ii) gated-off the fast electronics for a time of 10 msec;

iii) opened gates of memory circuits in order to store the information from all counters and all relevant electronic circuits of the trigger logic;

iv) started the reading out of all information related to the event after a delay of 0.5 msec; and

v) triggered the pulsed clearing field on the spark chambers.

2.5 Wire spark chambers

The wire spark chambers are identical to the ones used in an earlier experiment. Few details will be presented here, and we refer to the published description[2].

The rise-time of the negative high-voltage pulse on the chambers was typically 50 nsec, varying slightly with the size of the chambers. On each of the 33,300 wires was placed a ferrite core which flipped if a spark was present. The ferrite core read-out system[25] interrogated a group of 32 wires in 2 μsec. The probability that the same core would be fired on two consecutive pulsings of the chamber, the refiring probability, varied between 5 and 15% when the dead-time chosen for the chambers was 10 msec, being 15% for the telescopes W_1 and W_2 where the particle flux was high. The single track efficiency was typically 92%, giving an over-all chamber efficiency of typically 75%.

3. DATA ACQUISITION

3.1 On-line computer

The on-line computer was a Varian 620/i which was equipped with a ferrite core memory of 24 K. The task of the computer was twofold:

i) data acquisition

ii) control of the experimental apparatus.

The experimental data were stored on magnetic tapes. At this level no reduction of the data was done; the magnetic tapes consequently contained true raw data.

Checks of the functioning of the experiment were constantly done. Particularly the efficiency of detectors such as wire chambers, scintillation counters, and Čerenkov counters was regularly calculated.

3.2 Read-out system

The read-out system transferred the following quantities to the computer:

i) the content of 16 binary scalers;

ii) the counter information;

iii) the spark chamber data.

The binary scalers served particularly to count the number of incident particles of the different types. Each scaler occupied one word. All fired counters such as trigger counters, anticounters, beam hodoscopes, and Čerenkov counters were also registered. The information from one counter occupied one bit.

The spark chamber information was coded[26] and translated into binary words, which were presented to the data output lines. The data were packed in such a way that a cluster of a maximum of seven wires touched by the discharge occupied a 16-bit binary word.

At the end of a data file, decimal scalers were also read out. They contained the sum over all bursts of the incident particles registered by the binary scalers, which were reset after each burst. Data files for which the two system of scalers did not agree were not used in the cross-section calculation. This double system of scalers thus assured a correct measurement of the number of incident particles.

Each event occupied maximally 254 words, which were transmitted to the computer. The event information which was buffered in the computer, was written onto magnetic tape between machine bursts.

4. DATA ANALYSIS

During the main run, data were taken with the trigger conditions described in Section 2.4. During a short run the veto of forward-going pions was removed in order to cover also forward π^+p elastic scattering.

During some days of "parasitic" run some data on proton-proton elastic scattering were taken. The incident momentum for this short run was chosen to be 9 GeV/c.

For the whole experiment some 200 tapes were filled with data. Each tape contained around 50,000 events giving altogether for the experiment around 10^7 events. The final samples of elastic scattering events used for the cross-section calculations consisted of 65,000 π^+p events, 120,000 K^+p events, and 18,000 pp events. The analysis was done at CERN on the CDC 7600 computer.

4.1 Event reconstruction

The event reconstruction program proceeded according to the following scheme:

i) geometrical reconstruction;

ii) vertex reconstruction;

iii) kinematical test;

iv) momentum calculation;

v) kinematical fit with hypothesis test.

4.1.1 Geometrical reconstruction

To get a well-defined trajectory for the incident particle we required one counter fired in each of the four beam hodoscopes. If more than one counter was fired in one plane, ambiguities arose which were not accepted unless the two fired counters were adjacent.

For the tracks of the scattered particles we required at least three sparks to lie on a roughly straight line for each telescope projection. At this stage a time-saving filtering was done. The sparks supposed to define a straight line had to lie inside a road of predefined width before the least squares fit was performed. The road width, chosen from a study of the spark chamber resolution, was typically ±3 mm.

In order to save computer time (and memory space) we limited the number of sparks to eight sparks per chamber plane and eight tracks per projection. These restrictions reduced the number of events by about 20%.

The reconstructed tracks were required to match with the fired trigger counter. This test served to reduce spurious tracks.

4.1.2 Vertex reconstruction

Events having at least one track in both projections of W_1 and W_2 were retained. The vertex reconstruction was done in two steps. First the incident track was combined with the W_1 tracks, and a two-prong vertex was defined as the midpoint of the common normal.

Secondly, the normal from the two-prong vertex to the W_2 track was calculated. The three-prong vertex was defined as the point on this line, whose distance to the W_2 track (called R_3) was twice its distance to the two-prong vertex. If the distance R_3 was $\leq$ 10 mm the event was accepted. A distribution of R_3 is shown in Fig. 5.

We further required the events to be coplanar. The coplanarity index defined as the scalar product of the W_2 unit vector with the vector product of the unit vectors of the incident track and the W_1 track was required to be $\leq 8 \times 10^{-3}$. Figure 6 shows a distribution of the coplanarity index.

4.1.3 Kinematical test

The beam Čerenkov counters defined the signature of the incident particle. With this signature, the hypothesis of an elastic event could be tried. If the difference $\Delta\Theta$ between the calculated and measured values of the W_2 scattering angle was smaller than 8 mrad, the event was kept. Figure 7 shows a distribution of $\Delta\Theta$.

4.1.4 Momentum calculation

The spectrometer magnet was placed such that the forward-going particle would pass through it. As a consequence, particles scattered at very large angles were not momentum-analysed.

The main purpose of the spectrometer magnet was to filter out background particles with low momentum. The momentum measurement of one of the scattered particles proved to be a very good test of the elastic scattering hypothesis. Knowing the vertex point, the point in the middle of the magnet, and the deflection angle, the calculation of the momentum was done by an interpolation method[27]. If the difference Δp between the calculated and the measured momentum was greater than 1 GeV/c, the hypothesis was rejected. The precision of the momentum calculation $\Delta p/p$ was typically 3%. Figure 8 shows a distribution of Δp.

4.1.5 Kinematical fit and χ^2 test

In a fit which constrained the events to a three-prong vertex and to momentum and energy conservation, the χ^2 and the momenta of the scattered particles were calculated. If at this stage many hypotheses were possible for the event, the one with smallest χ^2 was chosen. Figure 9 shows a distribution of χ^2.

For the final sample of events used for the cross-section calculations, the cuts in χ^2 and Δp were restricted to $|\Delta p| < 0.8$ GeV/c and $\chi^2 < 30$.

4.2 Acceptance calculation

The acceptance of the experimental set-up was calculated with a Monte Carlo method. A number of randomly generated events was followed step by step through the detectors of the experiment. The proportion of originally generated events detected by the experimental apparatus defined the acceptance. Apart from the limited sizes of the scintillation counters, other effects intervened to reduce the acceptance. Such effects are:

i) absorption effects in the target and surrounding material;
ii) multiple scattering;
iii) decay of mesons.

The acceptance curves (as a function of the momentum transfer squared) are shown in Fig. 10 for π^+p elastic scattering. The contributions to the acceptance from the different telescope combinations are shown. Particles going through telescope T_3 are momentum-analysed, while particles through T_2 are usually not. One should note that the asymmetry between the acceptances in the forward and backward directions is due to the veto of the forward-going pions in part of the T_3 telescope. A more detailed description of the acceptance calculations can be found elsewhere[28,29].

4.3 Evaluation of the large-angle cross-sections

For the events without momentum measurement of any of the scattered particles the background situation was more complicated, and in our earlier published results[23,24] these events were not included. Calculations of the background have now been done[28] and these data are now included. The events without momentum measurement were of the kind T_2T_4 (one of the scattered particles in telescope T_2, the other in T_4) (see Figs. 1 and 10). A fraction of the events triggering telescope T_2 also went through T_3 and will consequently be momentum-analysed, and those events will be of the kind T_3T_4.

For events of the type T_2T_4 no momentum test of the outgoing particle was possible. As a consequence, the background was larger than for event samples with momentum calculation. In Fig. 11 is shown the probability distribution for π^+p events of the type T_2T_4 in the interval $5 < -t < 11$ $(GeV/c)^2$. When calculating the cross-sections, a cut was made at probability = 0.16, above which value the elastic hypothesis seemed to be the correct one. A correction for the good events rejected was made.

It is of importance to see if cross-sections calculated from events with different telescope combinations give the same result in overlapping t-intervals. The acceptance usually varies considerably near the edges (Fig. 10), and also the background can vary a lot depending on the trigger combination of the telescopes. In Fig. 12 we therefore show the differential cross-sections based on events with T_1T_3, T_3T_4, and T_2T_4 combinations, respectively. There is good agreement, which makes us believe that the acceptance calculation and the background estimate are correct.

Assuming the relative background in the K^+p large-angle sample to be the same as for π^+p, an upper limit of the cross-section at 90° c.m. scattering angle is calculated. In t-regions where no elastic K^+p events are found and the T_1T_3 or T_3T_4 acceptance is non-zero, the upper limit estimate is based on the hypothetical existence of 1 event.

4.4 Data corrections and background estimates

The main corrections of the data arose from inefficiency of the track detection. The efficiency for detecting a clean incident track without ambiguities was around 70%. The global efficiency to detect tracks in three spark chamber telescopes was typically 75%. (The track-finding efficiency for one chamber telescope was around 90%.) The spark chamber efficiencies were introduced for each data file as a function of the angle with the telescope.

Corrections were made for incorrect rejections of good events which could occur during the event reconstruction. This effect was estimated from studies of plots of events where sparks, tracks, and fired counters were indicated. We found that this effect amounted to typically 10%.

Loss due to random veto was estimated to be 5%. The demand of small Δp and good coplanarity of the events were an efficient means of strongly reducing the contamination of non-elastic events. The χ^2 distribution showed, however, that a small background existed. This background was evaluated from a study of χ^2-Δp plots. See Fig. 13.

The density of events outside the final cuts for good events was extrapolated into the region inside the cuts. This gave an estimate of the background in the final event samples, which was then corrected for. This procedure was done for different intervals of t. In Table 3 is collected the background estimates for the different reactions.

4.5 Consistency checks

Apart from checks of the acceptance in Section 4.3, subsamples of the data were compared in order to verify the data handling and the corrections on the data that were introduced. These samples were characterized by fairly large variations in the chamber efficiency, and in certain cases the data-taking conditions were quite different. After the introduction of the correction factors for the different samples, the cross-sections showed excellent agreement.

The over-all normalization error arose mainly from uncertainties in the correction factors described in Section 4.4. Some of them were introduced globally on the final results and thus did not influence the comparison of different samples. The over-all normalization error was estimated to ±15%.

5. EXPERIMENTAL RESULTS AND DISCUSSIONS

5.1 π^+p elastic scattering

Figure 14 shows the complete angular distribution for π^+p elastic scattering, and in Figs. 15-17 we show the details in smaller angular regions[1,2,4,8,9,30].

The t-distribution does not show any dip in the forward direction at $-t < 2.8$ (GeV/c)^2. At lower energies (Fig. 17) there is a pronounced dip at $t = -2.8$ (GeV/c)^2, which at 10 GeV/c has developed into a shoulder-like structure. At $-t = 4.8$ (GeV/c)^2 a second structure is observed with cross-sections typically an order of magnitude lower than in the region near $-t = 2.8$ (GeV/c)^2. In the interval $6 < -t < 14$ (GeV/c)^2 the statistics are not good enough to reveal any structures. The differential cross-sections are here at their lowest value around 1 nb/(GeV/c)^2. The backward peak does not show any structures in the t-interval covered by this experiment. [The well-known dip at $-u = 0.2$ (GeV/c)^2 is not covered.] In Table 4 the differential cross-sections are listed.

In Fig. 15 data at neighbouring momenta are compared in the forward direction. Good agreement between the experiment by Foley et al. at 8.8 and 10.8 GeV/c [9] and this experiment can be seen. A similar comparison is done in the backward direction in Fig. 16. One notices a good agreement where the precision of the measurements is high.

5.2 K^+p elastic scattering

The t-distribution obtained in this experiment is shown in Fig. 18. No structures are seen in the very forward and backward peaks. Around $-t = 3$ (GeV/c)^2 there is a break in the angular distribution. In the large t region few or no events were detected. In the intervals $5 < t < 7$ and $10 < -t < 13$ (GeV/c)^2, upper limits were calculated from 1 event of the type T_3T_4. In the interval $7 < -t < 10$ (GeV/c)^2 the upper limit was calculated assuming a background situation for the T_2T_4 events similar to the one valid for the corresponding π^+p sample (see Section 4.3). The differential cross-sections are listed in Table 5. Figure 19 shows the K^+p scattering for Foley et al. at 9.8 GeV/c [31] and this experiment in the forward region. The small deviations are well within the normalization errors of the experiments.

The forward t-distributions for K^+p elastic scattering are shown for some different energies in Fig. 20. The forward peak does not show any significant structures. The parametrization $d\sigma/dt = A\, e^{Bt}$ gives in the interval $0.45 < -t < 1.4$ (GeV/c)^2, $A = 10.8 \pm 0.2$ mb/(GeV/c)^2 and $B = 5.09 \pm 0.02$ (GeV/c)^2. At lower energies[2,14] a change of slope around $-t = 0.7$ (GeV/c)^2 is observed. Such a change would be difficult to observe in our data at 10 GeV/c because of the limited acceptance in the forward direction [$-t < 0.45$ (GeV/c)^2].

The energy dependence of the backward differential cross-sections is shown in Fig. 21 for $u = 0$, -0.5, and -1 (GeV/c)^2 [1,2,4,10,32-35]. Fits to the form $d\sigma/du = \text{const} \times s^{-\alpha}$ give, for incident momenta larger than 2 GeV/c, $\alpha = 3.9 \pm 0.2$ [2], 4.7 ± 0.3, and 5.1 ± 0.4 for $u = 0$, -0.5, and -1 (GeV/c)^2, respectively. There is an indication of a shrinkage of the backward peak. In a

simple Regge trajectory exchange picture one would expect an energy-dependence $d\sigma/du = s^{2\alpha_{eff}-2}$, where α_{eff} is the effective Regge trajectory. In Fig. 22 is shown the effective trajectory as a function of u. Our measured points fall on or very close to the extension of the Λ_α-Λ_γ trajectory, which is believed to dominate the baryon exchange in K^+p backward scattering.

5.3 pp elastic scattering

The proton-proton data were taken during a rather short run at 9.0 GeV/c incident momentum. We cover the interval $0.7 < -t < 5.0$ $(GeV/c)^2$. The result is presented in Fig. 23 together with data at neighbouring energies[9,36]. No significant structures are seen. The differential cross-sections are listed in Table 6.

The t-distributions for pp elastic scattering are shown in Fig. 24 for $|t| < 3$ $(GeV/c)^2$. For incident momenta < 30 GeV/c the t-distributions are very smooth[9,15,16,36-38]. However, at an incident momentum of around 10 GeV/c a distinct change between the steep forward peak and the more gentle decrease in the cross-section for $|t| > 1.5$ $(GeV/c)^2$ can be seen. At ISR energies the behaviour is radically different, with a very pronounced dip at $-t \approx 1.4$ $(GeV/c)^2$ followed by a maximum at $-t \approx 1.8$ $(GeV/c)^2$. These features are usually explained by diffraction mechanisms[39].

5.4 Comparison with parton-models

The constituent interchange model by Gunion et al.[19] predicts a differential cross-section for π^+p elastic scattering close to 90° c.m. scattering angle according to

$$\frac{d\sigma}{dt} = \frac{\sigma_0}{s^8} \frac{1+z}{(1-z)^4} \left[8(1+z)^{-2} + 1\right]^2 ,$$

where σ_0 is a constant

$$z = \cos \Theta_{cm} .$$

One notices the strong energy-dependence for fixed-angle scattering ($\propto s^{-8}$) and the energy-independent form for the angular distribution.

In Fig. 25 we show the parton model prediction for 5 and 10 GeV/c.

The constant σ_0 was taken to be 1.6×10^{-6} mb/$(GeV/c)^2$ in order to agree with the z = 0 value for π^+p elastic scattering at 10 GeV/c. At 10 GeV/c a good agreement is seen for $|\cos \Theta| < 0.6$, while at 5 GeV/c the disagreement is clear. As the domain of validity for parton models is confined to large values of s, t, and u, the disagreement may not be so surprising.

In Fig. 26 is shown the energy-dependence of differential cross-sections at fixed t, u, and c.m. scattering angle[2,3,5,30,40-43]. There the marked different energy dependence for different scattering regions is clearly displayed. The broken line corresponds to an s^{-8} decrease in cross-section, which for $s > 8$ GeV^2 seems to be in accord with the experimental findings.

For K^+p large-angle elastic scattering the parton model mentioned above predicts the following behaviour:

$$\frac{d\sigma}{dt} = \frac{\sigma_0}{s^8} \frac{1 + z}{(1 - z)^4} 64(1 + z)^{-4} .$$

In Fig. 27 the data at 5 and 10 GeV/c are shown together with this parton model prediction. The constant σ_0 is the same as for π^+p elastic scattering. Already at 5 GeV/c one notices a rather good agreement for $|\cos \Theta| < 0.5$. At 10 GeV/c only upper limits for the differential cross-section around 90° c.m. exist.

The energy dependence for the 90° c.m. cross-section is shown in Fig. 28 [2,11,32,34,44-47].

For proton-proton elastic scattering the predicted energy dependence for the 90° c.m. cross-section varies between the different parton models. The constituent interchange model by Gunion et al.[19] predicts an s^{-12} dependence, while a model by Brodsky et al.[20] using simple counting of the number of quarks predicts an s^{-10} dependence. In Fig. 29 is shown the energy dependence for the proton-proton cross-section at 90° c.m. scattering angle[15,16,37,38,48-52]. It is clear that an s^{const} dependence of the cross-section does not describe the experimental data very well in the energy interval explored up to now.

5.5 Elastic scattering around 10 GeV/c

Figure 30 shows the t-distributions for π^+p and K^+p elastic scattering around 10 GeV/c. The π^-p data come from Owen et al.[1] at 9.8 GeV/c. The similarities between π^+p and π^-p scattering are the most striking, even though some differences also exist. The similarities between π^+p and π^-p were already noticed at 5 GeV/c [2], where the two reactions were studied with the same set-up. The $\pi^\pm p$ distributions diverge at large angles and particularly in the backward region, where the different Regge exchanges (N and Δ exchange for π^+p, and only Δ exchange for π^-p scattering) still give rise to different cross-sections. At large angles the K^+p data are non-existent or very imprecise, but in other regions the data tend to follow the pion distributions.

Acknowledgements

We thank P. Anzoli, B. Mouellic and D. Ploujoux for their excellent technical support, and R. Kiesler for his very capable handling of the complicated electronic system.

As this experiment was the first one to be analysed on the CDC 7600 computer at CERN, many major debugging problems arose, which were efficiently solved with the appreciable help of C. Letertre and G. Frigo from the CERN Data Handling Division.

REFERENCES

1) D.P. Owen, F.C. Peterson, J. Orear, A.L. Read, D.G. Ryan, D.H. White, A. Ashmore, C.J.S. Damerell, W.R. Frisken and R. Rubinstein, Phys. Rev. 181 (1969) 1794.

2) A. Eide, P. Lehmann, A. Lundby, C. Baglin, P. Briandet, P. Fleury, P.J. Carlson, K.E. Johansson, M. Davier, V. Gracco, R. Morand and D. Treille, Nuclear Phys. B60 (1973) 173-220.

3) C.T. Coffin, N. Dikmen, L. Ettlinger, D. Meyer, A. Saulys, K. Terwilliger and D. Williams, Phys. Rev. 159 (1967) 1169.

4) A. Bashian, G. Finocchiaro, G.C. Fischer, M.L. Good, O. Guisan, J. Kirz, Y.Y. Lee and D.D. Reader, Phys. Rev. D 9 (1974) 3193.

5) W.F. Baker, K. Berkelman, P.J. Carlson, G.P. Fisher, P. Fleury, D. Hartill, K. Kalbach, A. Lundby, S. Mukhin, R. Nierhaus, K.P. Pretzl and J. Woulds, Nuclear Phys. B25 (1971) 385.

6) Yu.M. Antipov, G. Ascoli, R. Busnello, G. Damgaard, M.N. Kienzle-Focacci, W. Kienzle, R. Klanner, L.G. Landsberg, A.A. Lebedev, C. Lechanoine, P. Lecomte, M. Martin, V. Roinishvili, R.D. Sard, A. Weitsch and F.A. Yotch, Nuclear Phys. B57 (1973) 333.

7) P. Cornillon, G. Grindhammar, J.H. Klems, P.O. Mazur, J. Orear and J. Peoples, Phys. Rev. Letters 30 (1973) 403.

8) R. Rubinstein, P. Cornillon, G. Grindhammar, J.H. Klems, P.O. Mazur, J. Orear, J. Peoples and W. Faissler, Phys. Rev. Letters 30 (1973) 1010.

9) K.J. Foley, S.J. Lindenbaum, W.A. Love, S. Ozaki, J.J. Russel and L.C.L. Yuan, Phys. Rev. Letters 11 (1963) 425.

10) P.L. Jain, T. Swissler, M. Primer, R.K. Shirpuri, D. Evans, I.L. Stone, T. Ferbel, P.F. Slattery and H. Yuta, Nuclear Phys. B19 (1970) 568.

11) C.W. Akerlof, K.S. Han, D.J. Meyer, P. Schmueser, P.N. Kirk, D.R. Rust, C.E. Ward, D.D. Yovanovitch and S.M. Pruss, Phys. Rev. Letters 26 (1971) 1278.

12) I. Ambats, D.S. Ayres, R. Diebold, A.F. Greene, S.L. Kramer, A. Lesnik, D.R. Rust, C.E.W. Ward, A.B. Wicklund and D.D. Yovanovitch, Phys. Rev. D 9 (1974) 1179.

13) C.W. Akerlof, R. Kotthaus, J.A. Koschik, R.L. Loveless, D.I. Meyer, I. Ambats, W.T. Meyer, C.E.W. Ward, D.P. Eartly, R.A. Lundy, S.M. Pruss, D.D. Yovanovitch and D.R. Rust, Report UM HE 74-20 (1974).

14) H. Yuta, G. Bock, B. Musgrave, P. Peeters, P. Schreiner and J. Whitmore, Report ANL/HEP 7419 (1974).

15) J.V. Allaby, F. Binon, A.N. Diddens, P. Duteil, A. Klovning, R. Meunier, J.P. Peigneux, E.J. Sacharidis, K. Schlüpmann, M. Spighel, J.P. Stroot, A.M. Thorndike and A.M. Wetherell, Phys. Letters 28B (1968) 67.

16) J.V. Allaby, A.N. Diddens, R.W. Dobinson, A. Klovning, J. Litt, L.S. Rochester, K. Schlüpmann and A.M. Wetherell, Nuclear Phys. B52 (1973) 316.

17) A. Böhm, B. Bozzo, R. Ellis, H. Foeth, M.J. Ferrero, G. Maderni, B. Naroska, C. Rubbia, G. Sette, A. Staude, P. Strolin and G. De Zorzi, Phys. Letters 49B (1974) 491.

18) CERN-Hamburg-Orsay-Vienna Collaboration, Proc. 17th Internat. Conf. on High-Energy Physics, London, 1974 (Rutherford Lab., Chilton, 1974), p. I-30.

19) J.F. Gunion, S.J. Brodsky and R. Blankenbecler, Phys. Rev. D 8 (1973) 287.

20) S.J. Brodsky and G.R. Farrar, SLAC-report, SLAC-PUB 1290 (1973).

21) G. Preparata, Report TH-1836 CERN (1974).

22) T. Buran et al., K^-p and $\bar{p}p$ elastic scattering and two-body annihilations at 6.2 GeV/c, Proc. 17th Internat. Conf. on High-Energy Physics, London, 1974 (Rutherford Lab., Chilton, 1974).

23) C. Baglin, P. Briandet, P.J. Carlson, B. d'Almagne, A. Eide, P. Fleury, V. Gracco, E. Johansson, P. Lehmann, A. Lundby, S. Mukhin, A. Navarro-Savoy, A. Pevsner, F. Richard, G. de Rosny, L. Staurset and D. Treille, Phys. Letters 47B (1973) 85.

24) C. Baglin, P. Briandet, P.J. Carlson, B. d'Almagne, A. Eide, P. Fleury, V. Gracco, E. Johansson, P. Lehmann, A. Lundby, S. Mukhin, A. Navarro-Savoy, A. Pevsner, F. Richard, G. de Rosny, L. Staurset and D. Treille, Phys. Letters 47B (1973) 89.

25) J. Lindsay and I. Pizer, Proc. Internat. Symp. on Nuclear Electronics, Versailles, 1968 (La Documentation française, Paris, 1969), t.3, p. 22-1.

26) R.L. Bloch, P. Briandet and A. Simon, SCRO spark chamber read-out, TYPE 041, CERN-NP CAMAC Note 19-00 Nov. 1970.

27) C. Lechanoine, M. Martin and H. Wind, Nuclear Instrum. Methods 69 (1969) 122.

28) E. Johansson, Hadron-hadron elastic scattering and annihilation reactions at 5 and 10 GeV/c, Thesis, University of Stockholm, 1974.

29) A. Savoy-Navarro, Mesure de la section efficace différentielle à grands angles des processus de diffusions élastiques π^+p et K^+p à 10 GeV/c, Thesis, University of Strasbourg, 1973.

30) B.B. Brabson, R.R. Crittenden, R.M. Heinz, R.C. Kammerud, H.A. Neal, H.W. Paik and R.A. Sidwell, Phys. Rev. Letters 25 (1970) 553.

31) K.J. Foley, J.J. Lindenbaum, W.A. Love, S. Ozaki, J.J. Russel and L.C.L. Yuan, Phys. Rev. Letters 11 (1963) 503.

32) J. Whitmore, G.S. Abrams, L. Eisenstein, J. Kim, T.A. O'Halloran, jr. and W. Shufeldt, Phys. Rev. D 3 (1971) 1092.

33) A. Seidl, Phys. Rev. D 7 (1973) 621.

34) J.N. MacNaughton, L. Feinstein, F. Marcelja and G. Trillings, Nuclear Phys. B14 (1969) 237.

35) J. Bartsch, M. Deutschmann, G. Kraus, H. Böttcher, U. Gensch, J. Kaltwasser, D. Pose, J.R. Campbell, V.T. Cocconi, J.D. Hansen, G. Kellner, W. Kittel, S. Matsumoto, D.R.O. Morrison, R. Stroynowski, J.B. Whittaker, N.C. Barford, G.A. Grammatikakis, B.R. Kumar, A.W. Mutalib, A. Fröhlich, P. Porth, P. Schmid and H. Wahl, Nuclear Phys. B29 (1971) 398.

36) J.V. Allaby et al., CERN 68-7 (1968), p. 580.

37) C.M. Ankenbrandt, A.R. Clark, B. Cork, T. Elioff, L.T. Kerth and W.A. Wenzel, Phys. Rev. 170 (1968) 1223.

38) C. Clyde, UCRL 16275 (1966).

39) L. Durand and R. Lipes, Phys. Rev. Letters 20 (1968) 637.

40) D.R. Rust, P.N. Kirk, R.A. Lundy, C.E.W. Ward, D.D. Yovanovitch, S.M. Pruss, C.W. Akerlof, K.S. Han, D.I. Meyer and P. Schmueser, Phys. Rev. Letters 24 (1970) 1361.

41) M.N. Focacci, S. Focardi, G. Giacomelli, P. Serra, M.P. Zerbetto and L. Monari, Phys. Letters 19 (1965) 441.

42) G. Giacomelli, P. Lugaresi-Serra, G. Mandrioli, A.M. Rossi, F. Griffiths, J.S. Hughes, D.A. Jacobs, R. Jennings, B.C. Wilson, G. Ciapetti, V. Costantini, G. Martellotti, D. Zanello, E. Castelli and M. Sessa, Nuclear Phys. B20 (1970) 301.

43) J. Banaigs, J. Berger, C. Bonnel, J. Duflo, L. Goldzahl, F. Plouin, W.F. Baker, P.J. Carlson, V. Chabaud and A. Lundby, Nuclear Phys. B8 (1968) 31.

44) W. De Baere, J. Debaisieux, P. Dufour, F. Grard, J. Heughebaert, L. Pape, P. Peeters, F. Verbeure, R. Windmolders, R. George, Y. Goldschmidt-Clermont, V.P. Henri, B. Jongejans, D.W.G. Leith, A. Moisseev, F. Muller, J.M. Perreau and V. Yarba, Nuovo Cimento 45A (1966) 885.

45) M.G. Albrow, S. Andersson-Almehed, B. Bosnjaković, C. Daum, F.C. Erné, Y. Kimura, J.P. Lagnaux, J.C. Sens, F. Udo and P. Wagner, Nuclear Phys. B30 (1971) 273.

46) J.A. Danysz, M. Spiro, A. Verglas, J.M. Brunet, J.L. Narjoux, B. Penney, G. Thompson, P.H. Lewis, J.E. Allen and P.V. March, Nuclear Phys. B14 (1969) 161.

47) J. Debaiseux, F. Grard, J. Heughebaert, L. Pape, R. Windmolders, R. George, Y. Goldschmidt-Clermont, V.P. Henri, D.W.G. Leith, G.R. Lynch, F. Muller, J.M. Perreau, G. Otter and P. Sällström, Nuovo Cimento 43A (1966) 142.

48) J.V. Allaby, A.N. Diddens, A. Klovning, E. Lillethun, E.J. Sacharidis, K. Schlüpmann and A.M. Wetherell, Phys. Letters 27B (1968) 49.

49) J.V. Allaby, G. Cocconi, A.N. Diddens, A. Klovning, G. Matthiae, E.J. Sacharidis and A.M. Wetherell, Phys. Letters 25B (1967) 156.

50) B.A. Brabson, R.R. Crittenden, R.M. Heinz, R.C. Kammerud, H.A. Neal, H.W. Paik, R.A. Sidwell and K.F. Suen, Phys. Rev. Letters 23 (1969) 1306.

51) B.A. Ryan, A. Kanofsky, T.J. Devlin, R.E. Mischke and P.F. Sheperd, Phys. Rev. D 3 (1971) 1.

52) D.T. Williams, I.J. Bloodworth, E. Eisenhandler, W.R. Gibson, P.I.P. Kalmus, L.C.Y. Lee Chi Kwong, G.T.J. Arnison, A. Astbury, S. Gjesdal, E. Lillethun, B. Stave, O. Ullaland and I.L. Watkins, Nuovo Cimento 8A (1972) 447.

Table 1

The over-all size and the number of elements for each scintillation counter array

Scintillation counter array	Over-all size horizontal by vertical (cm^2)	Number of elements	
		Vertical	Horizontal
T_1	213 × 60	17	4
T_2	70 × 40	7	2
T_3	170 × 75	11	8
T_4	80 × 75	4	2

Table 2

Particle signatures given by the beam-Čerenkov counters

Signature	Combination of Čerenkov counters
π	$(C_1 + C_3) \cdot C_2$
K	$C_1 \cdot \bar{C}_2 \cdot C_3$
p	$\bar{C}_1 \cdot \bar{C}_2 \cdot \bar{C}_3$

Table 3

Background estimations for the pion, kaon, and proton samples

t-interval $(GeV/c)^2$	Pion background (%)
$-t \leq 7$	5
$7 < -t \leq 10$	30
$10 < -t < 16$	15
$-t \geq 16$	5

t-interval $(GeV/c)^2$	Kaon background (%)
$-t \leq 2$	3
$2 < -t \leq 5$	4
$-t \geq 13$	20

t-interval $(GeV/c)^2$	Proton background (%)
$-t \leq 2$	4
$-t > 2$	6

Table 4

Differential cross-sections for $\pi^+ p$ elastic scattering at 10 GeV; $s = 19.667\ (GeV)^2$ and $u = -t - 17.867\ (GeV/c)^2$. The errors quoted are statistical and represent one standard deviation. The over-all normalization error is ±15%.

$-t$ $(GeV/c)^2$	Δt	$d\sigma/dt$ $\mu b/(GeV/c)^2$	Error
0.42	0.04	1276	65
0.46	0.04	1144	61
0.50	0.04	834	44
0.54	0.04	614	34
0.58	0.04	520	30
0.62	0.04	308	13
0.66	0.04	292	13
0.70	0.04	215	10
0.74	0.04	161.6	8.2
0.78	0.04	148.0	8.2
0.82	0.04	123.0	7.1
0.86	0.04	94.5	5.9
0.90	0.04	86.7	5.7
0.95	0.06	58.9	3.6
1.01	0.06	49.5	3.3
1.07	0.06	40.0	3.0
1.14	0.08	28.5	2.1
1.22	0.08	19.2	1.7
1.30	0.08	16.1	1.5
1.38	0.08	12.9	1.3
1.46	0.08	8.7	1.1
1.55	0.10	5.14	0.12
1.65	0.10	3.88	0.10
1.75	0.10	2.695	0.079
1.85	0.10	1.922	0.064
1.95	0.10	1.179	0.049
2.05	0.10	0.797	0.039
2.15	0.10	0.493	0.031
2.25	0.10	0.327	0.026
2.35	0.10	0.199	0.020
2.45	0.10	0.130	0.017
2.55	0.10	0.065	0.012
2.65	0.10	0.072	0.013

Table 4 (contd)

$-t$ $(GeV/c)^2$	Δt	$d\sigma/dt$ $\mu b/(GeV/c)^2$	Error
2.75	0.10	0.046	0.010
2.85	0.10	0.056	0.011
2.95	0.10	0.042	0.010
3.05	0.10	0.049	0.011
3.15	0.10	0.058	0.013
3.25	0.10	0.043	0.010
3.35	0.10	0.043	0.011
3.45	0.10	0.031	0.009
3.55	0.10	0.045	0.012
3.65	0.10	0.033	0.011
3.75	0.10	0.0182	0.0069
3.85	0.10	0.0205	0.0073
3.95	0.10	0.038	0.011
4.05	0.10	0.0069	0.0034
4.20	0.20	0.0187	0.0047
4.40	0.20	0.0124	0.0043
4.60	0.20	0.0103	0.0034
4.80	0.20	0.0054	0.0024
5.00	0.20	0.0108	0.0036
5.20	0.20	0.0146	0.0049
5.40	0.20	0.0126	0.0042
5.75	0.50	0.0057	0.0017
6.5	1.0	0.0020	0.0007
7.5	1.0	0.0026	0.0006
8.5	1.0	0.0024	0.0006
9.6	1.2	0.0009	0.0004
11.10	1.80	0.0015	0.0006
13.00	2.00	0.0015	0.0005
14.50	1.00	0.0055	0.0010
15.05	0.10	0.0050	0.0029
15.15	0.10	0.0151	0.0061
15.25	0.10	0.0091	0.0035
15.35	0.10	0.0315	0.0070
15.45	0.10	0.0329	0.0070
15.55	0.10	0.0174	0.0047
15.65	0.10	0.0230	0.0055
15.75	0.10	0.0372	0.0073
15.85	0.10	0.0372	0.0072

Table 4 (contd)

$-t$ $(GeV/c)^2$	Δt	$d\sigma/dt$ $\mu b/(GeV/c)^2$	Error
15.95	0.10	0.0410	0.0071
16.05	0.10	0.076	0.010
16.15	0.10	0.076	0.010
16.25	0.10	0.103	0.012
16.35	0.10	0.144	0.015
16.45	0.10	0.154	0.015
16.55	0.10	0.196	0.017
16.65	0.10	0.203	0.018
16.75	0.10	0.256	0.020
16.85	0.10	0.339	0.024
16.95	0.10	0.400	0.026
17.05	0.10	0.422	0.039
17.15	0.10	0.595	0.050
17.25	0.10	0.694	0.056

Table 5

Differential cross-sections for K^+p elastic scattering at 10 GeV/c; $s = 19.91$ GeV^2 and $u = -t - 17.704$ (GeV/c)^2. The errors given are statistical and represent one standard deviation. The over-all normalization error is ±15%.

$-t$ (GeV/c)^2	Δt	$d\sigma/dt$ μb/(GeV/c)^2	Error	$-t$ (GeV/c)^2	Δt	$d\sigma/dt$ μb/(GeV/c)^2	Error
0.45	0.02	1131	36	1.13	0.02	33.6	2.2
0.47	0.02	1009	32	1.15	0.02	29.3	2.0
0.49	0.02	961	21	1.17	0.02	28.3	2.0
0.51	0.02	838	27	1.19	0.02	22.3	1.7
0.53	0.02	729	23	1.21	0.02	22.3	1.6
0.55	0.02	702	23	1.23	0.02	21.5	1.7
0.57	0.02	624	21	1.25	0.02	17.8	1.5
0.59	0.02	575	19	1.27	0.02	17.1	1.4
0.61	0.02	454	11	1.29	0.02	13.9	1.3
0.63	0.02	435	11	1.31	0.02	12.8	1.2
0.65	0.02	386	10	1.33	0.02	11.8	1.2
0.67	0.02	340	9	1.35	0.02	10.1	1.0
0.69	0.02	315	8	1.37	0.02	9.9	1.0
0.71	0.02	282	8	1.39	0.02	8.7	1.0
0.73	0.02	251	6	1.41	0.02	9.3	1.0
0.75	0.02	216	6	1.43	0.02	8.8	1.0
0.77	0.02	216	6	1.45	0.02	7.7	0.9
0.79	0.02	193	6	1.47	0.02	6.2	0.8
0.81	0.02	169	5	1.49	0.02	5.4	0.8
0.83	0.02	156	5	1.52	0.04	4.3	0.5
0.85	0.02	141	5	1.56	0.04	4.3	0.5
0.87	0.02	132	5	1.60	0.04	3.2	0.4
0.89	0.02	120	4	1.64	0.04	2.7	0.4
0.91	0.02	102	4	1.68	0.04	1.65	0.24
0.93	0.02	93.6	3.5	1.72	0.04	1.75	0.30
0.95	0.02	82.4	3.3	1.77	0.06	1.34	0.22
0.97	0.02	77.8	3.2	1.83	0.06	0.95	0.19
0.99	0.02	67.7	2.9	1.89	0.06	0.69	0.16
1.01	0.02	64.7	3.4	1.96	0.06	0.53	0.13
1.03	0.02	59.3	3.2	2.1	0.2	0.36	0.07
1.05	0.02	49.6	2.8	2.35	0.3	0.17	0.04
1.07	0.02	48.7	2.8	2.65	0.3	0.087	0.029
1.09	0.02	42.5	2.6	3.05	0.5	0.048	0.017
1.11	0.02	35.5	2.3	3.55	0.5	0.040	0.014

Table 5 (contd)

$-t$ $(GeV/c)^2$	Δt	$d\sigma/dt$ $\mu b/(GeV/c)^2$	Error	$-t$ $(GeV/c)^2$	Δt	$d\sigma/dt$ $\mu b/(GeV/c)^2$	Error
4.4	1.2	0.018	0.007	16.25	0.5	0.030	0.009
6	2	< 0.0020		16.60	0.2	0.081	0.026
8.5	3	< 0.0009		16.80	0.2	0.079	0.024
11.5	3	< 0.0012		17.00	0.2	0.16	0.04
14.25	2.5	0.004	0.002	17.20	0.2	0.20	0.07
15.75	0.5	0.027	0.009				

Table 6

Differential cross-sections for pp elastic scattering at 9.0 GeV/c; $s = 18.74\ GeV^2$. The errors given are statistical and represent one standard deviation. The over-all normalization error is ±15%.

$-t$ $(GeV/c)^2$	Δt	$d\sigma/dt$ $\mu b/(GeV/c)^2$	Error
0.71	0.02	290	15
0.73	0.02	286	15
0.75	0.02	234	12
0.77	0.02	249	13
0.79	0.02	202	11
0.81	0.02	214	12
0.83	0.02	182	10
0.85	0.02	156	9.4
0.87	0.02	138	8.7
0.89	0.02	121	7.7
0.91	0.02	107	7.1
0.93	0.02	113	7.6
0.95	0.02	90.3	6.5
0.97	0.02	80.5	5.9
0.99	0.02	78.4	6.0
1.01	0.02	69.8	5.6
1.03	0.02	64.5	5.2
1.05	0.02	58.0	5.1
1.07	0.02	41.8	4.0
1.09	0.02	39.8	4.0
1.15	0.10	35.0	1.7
1.25	0.10	22.9	1.4
1.35	0.10	17.7	1.3
1.45	0.10	12.6	1.0
1.55	0.10	9.69	0.94
1.65	0.10	12.17	1.14
1.75	0.10	8.59	0.93
1.85	0.10	6.70	0.77
1.95	0.10	5.93	0.76
2.10	0.20	4.17	0.42
2.30	0.20	3.11	0.37
2.50	0.20	3.09	0.41
2.75	0.30	2.26	0.28

Table 6 (contd)

$-t$ $(GeV/c)^2$	Δt	$d\sigma/dt$ $\mu b/(GeV/c)^2$	Error
3.05	0.30	1.27	0.23
3.35	0.30	1.18	0.27
3.65	0.30	1.19	0.26
4.00	0.40	0.44	0.15
4.40	0.40	0.32	0.10
4.80	0.40	0.17	0.10

Figure captions

Fig. 1 : Layout for the 10 GeV/c experiment: S_1-S_4 are scintillation counters. C_1-C_3 are Čerenkov counters, T_1-T_4 are counter telescopes, W_1-W_4 are spark chamber telescopes, V_1, V_2 are veto counters and M is the spectrometer magnet. The scale indicated is not valid for the incident beam up to the target.

Fig. 2 : Layout of the secondary beam d_{30}: Q_1-Q_7 are quadrupoles, BM_1-BM_4 are bending magnets. Production angle (Θ_1) is 83 mrad.

Fig. 3 : Pressure curves for Čerenkov counter C_2: S is the fourfold coincidence $S_1 \cdot S_2 \cdot S_3 \cdot S_4$ and represents an incident particle of any kind. For the full line, X is the three fold coincidence $C_1 \cdot \bar{C}_2 \cdot C_3$; for the broken line, $X = (C_1 + C_3)C_2$. C_1 and C_3 were operated at a pressure of 11.6 atm.

Fig. 4 : Pressure curve for the Čerenkov counters C_1 and C_3: S is the fourfold coincidence $S_1 \cdot S_2 \cdot S_3 \cdot S_4$ and represents an incident particle of any kind. C_2 had a pressure of 7 atm.

Fig. 5 : Distribution of the distance R_3. The arrow indicates the maximum accepted value.

Fig. 6 : Distribution of the coplanarity index R_{cop}. The arrows indicate the maximum accepted values.

Fig. 7 : Distribution of $\Delta\Theta$. The arrows indicate the maximum accepted values.

Fig. 8 : Distribution of Δp for K^+p elastic event.

Fig. 9 : χ^2 distribution for 6000 elastic π^+p events.

Fig. 10 : Acceptance curves for π^+p elastic scattering for different telescope combinations. The full curve is T_1T_3 combination, the broken line the T_3T_4, and the dotted line the T_2T_4. In part of T_3 the pion is not allowed, giving a reduced acceptance in the forward direction.

Fig. 11 : Probability distribution for π^+p events in the interval $5 < -t < 11$ $(GeV/c)^2$. The events are of the type T_2T_4, and hence no momentum test is possible.

Fig. 12 : Differential cross-sections for π^+p elastic scattering at 10 GeV/c in the large-angle region. The results for three different telescope combinations are shown.

Fig. 13 : Plot of χ^2-Δp for 250 elastic π^+p events in the region $2 < -t < 4$ $(GeV/c)^2$.

Fig. 14 : Full angular distribution for π^+p elastic scattering at 10 GeV/c measured in this experiment.

Fig. 15 : Differential cross-sections for π^+p elastic scattering in the forward region. The data points come from this experiment at 10 GeV/c and from Foley et al. (Ref. 9) at 8.8 and 10.8 GeV/c.

Fig. 16 : Differential cross-sections for π^+p elastic scattering in the backward region. The filled circles are data points from this experiment at 10 GeV/c, the open circles are data points from Owen et al. (Ref. 1) at 9.85 GeV/c, and the open squares are from Bashian et al. (Ref. 4) at 10 GeV/c.

Fig. 17 : Differential cross-sections for π^+p elastic scattering for different incident momenta. The curves at 3 and 4 GeV/c come from Brabson et al. (Ref. 30), the open circles from Eide et al. (Ref. 2) at 5 GeV/c, the filled squares from this experiment at 10 GeV/c, and the open squares come from Rubinstein et al. (Ref. 8).

Fig. 18 : Differential cross-section for K^+p elastic scattering at 10 GeV/c measured in this experiment.

Fig. 19 : Differential cross-sections for K^+p elastic scattering in the forward region. Data from this experiment and from Foley et al. (Ref. 31).

Fig. 20 : Differential cross-sections for K^+p elastic scattering for different incident momenta. The data points are from Eide et al. (Ref. 2) at 5 GeV/c (filled triangles), from Foley et al. (Ref. 31) at 9.8 GeV/c (open circles), from this experiment at 10 GeV/c (filled circles) and from Jain et al. (Ref. 10) at 12.7 GeV/c (open squares).

Fig. 21 : Differential cross-sections at $u = -0.5$ and -1 $(GeV/c)^2$ as a function of the total energy in the c.m. system squared. Also shown is a line corresponding to the behaviour at $u = 0$ (Ref. 2). The straight lines through the data points represent fits discussed in the text. Data from Refs. 1, 2, 4, 10, 32-35.

Fig. 22 : The effective trajectory α_{eff} as a function of u derived from the fits discussed in the text (filled squares). The straight line is drawn through the states Λ_α (filled circles) and Λ_γ (open circles).

Fig. 23 : Differential cross-sections for pp elastic scattering. The round circles are from Foley et al. (Ref. 9) at 8.8 GeV/c, the filled circles are from this experiment at 9.0 GeV/c, and the open squares are from Allaby et al. (Ref. 36) at 9.2 GeV/c.

Fig. 24 : Differential cross-sections for pp elastic scattering. The data are:

2.98	GeV/c	Ankenbrandt et al.	(Ref. 37)
3	GeV/c	Clyde et al.	(Ref. 38)
5	GeV/c	Clyde et al.	(Ref. 38)
7	GeV/c	Clyde et al.	(Ref. 38)
8.8	GeV/c	Foley et al.	(Ref. 9)
9.0	GeV/c	This experiment	
9.2	GeV/c	Allaby et al.	(Ref. 36)
14.2	GeV/c	Allaby et al.	(Ref. 16)
19.2	GeV/c	Allaby et al.	(Ref. 15)
24.0	GeV/c	Allaby et al.	(Ref. 16)

The ISR experiments are indicated with lines:
--- $\sqrt{s}$ = 23, 307 GeV/c Böhm et al. (Ref. 17)
—— $\sqrt{s}$ = 53, 1500 GeV/c Nagy et al. (Ref. 18)
... $\sqrt{s}$ = 62, 1947 GeV/c Böhm et al. (Ref. 17)

Fig. 25 : The differential cross-sections for π^+p elastic scattering at 5 GeV/c (Ref. 2) and 10 GeV/c measured in this experiment as function of cos Θ_{cm}. The curves are the predictions of the parton model discussed in the text. The full and broken lines are the predictions at 5 and 10 GeV/c, respectively.

Fig. 26 : The energy dependence of the differential π^+p elastic cross-sections at fixed values of t and u and at 90° c.m. angle. The curves are hand-drawn. The broken straight line corresponds to an s^{-8} decrease in cross-section. The data come from this experiment and from Refs. 2, 3, 5, 30, 40-43.

Fig. 27 : The differential cross-sections for K^+p elastic scattering at 5 GeV/c (Ref. 2) and 10 GeV/c measured in this experiment as a function of cos Θ_{cm}. The curves are the predicitions of the parton model discussed in the text. The full and broken lines are the predictions at 5 and 10 GeV/c, respectively. For the estimate of the K^+p upper limits at 10 GeV/c, see Section 4.3.

Fig. 28 : Energy dependence for the K^+p differential cross-section at 90° c.m. The broken line corresponds to an s^{-8} decrease of the cross-sections. Data from Refs. 2, 11, 32, 34, 44-47, and this experiment.

Fig. 29 : Energy dependence for proton-proton elastic scattering at 90° c.m. The full line corresponds to an s^{-10} decrease of the cross-sections and the broken line corresponds to an s^{-12} decrease of the cross-sections. Data from Refs. 15, 16, 37, 38, 48-52.

Fig. 30 : The differential cross-sections for $\pi^{\pm}p$ and K^+p elastic scattering reactions around 10 GeV/c are shown. The data come from Owen et al. (Ref. 1) and this experiment. The upper limits refer to K^+p scattering at 10 GeV/c (see Section 4.3).

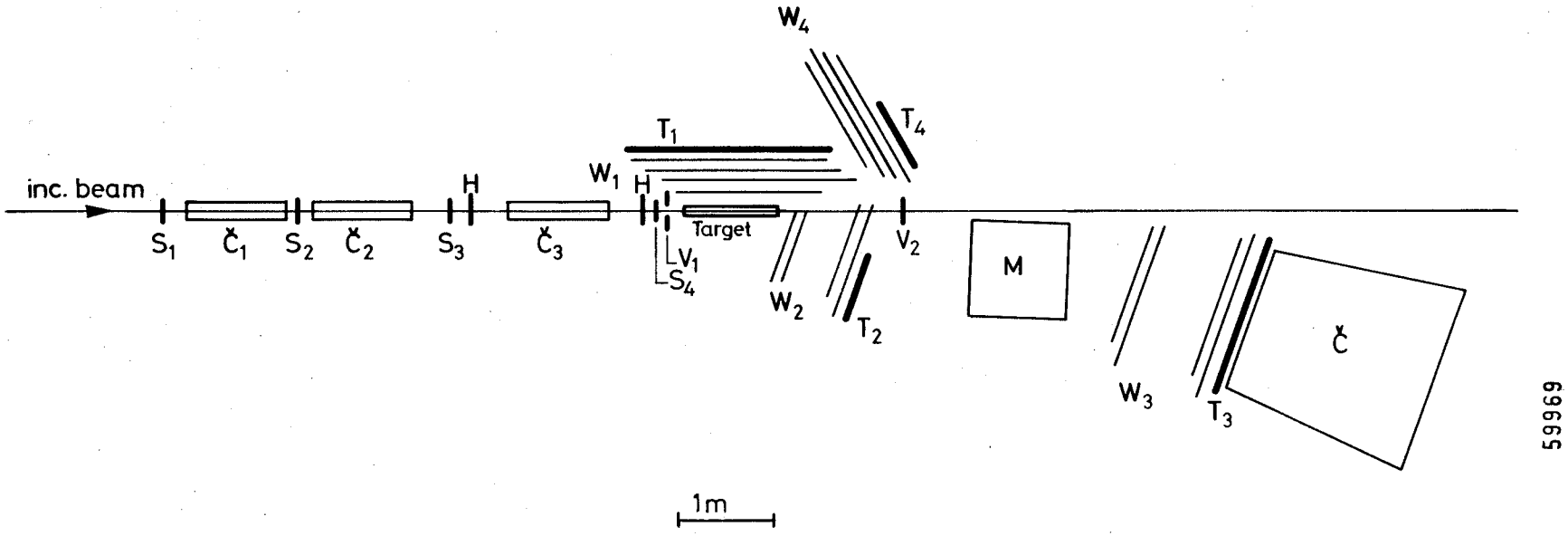
W4
T4
T1
W1
H
H
inc. beam
S1
Č1
S2
Č2
S3
Č3
Target
V1
S4
V2
W2
T2
M
W3
T3
Č
1m
59969

Fig. 1

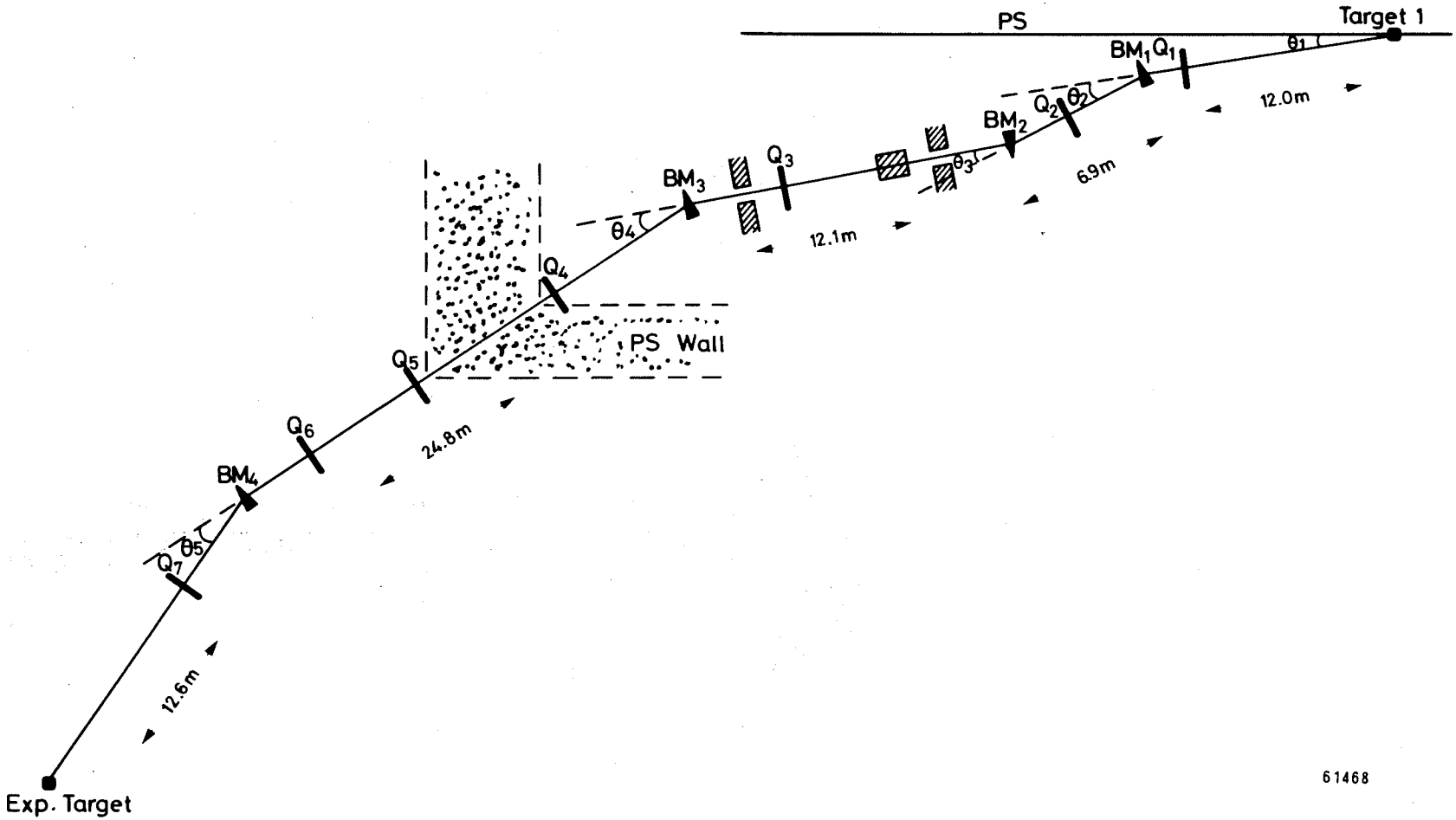
PS
Target 1
BM1 Q1
θ1
12.0m
BM2
Q2
θ2
6.9m
BM3
Q3
θ3
12.1m
θ4
Q4
PS Wall
Q5
24.8m
Q6
BM4
Q7
θ5
12.6m
Exp. Target
61468

Fig. 2

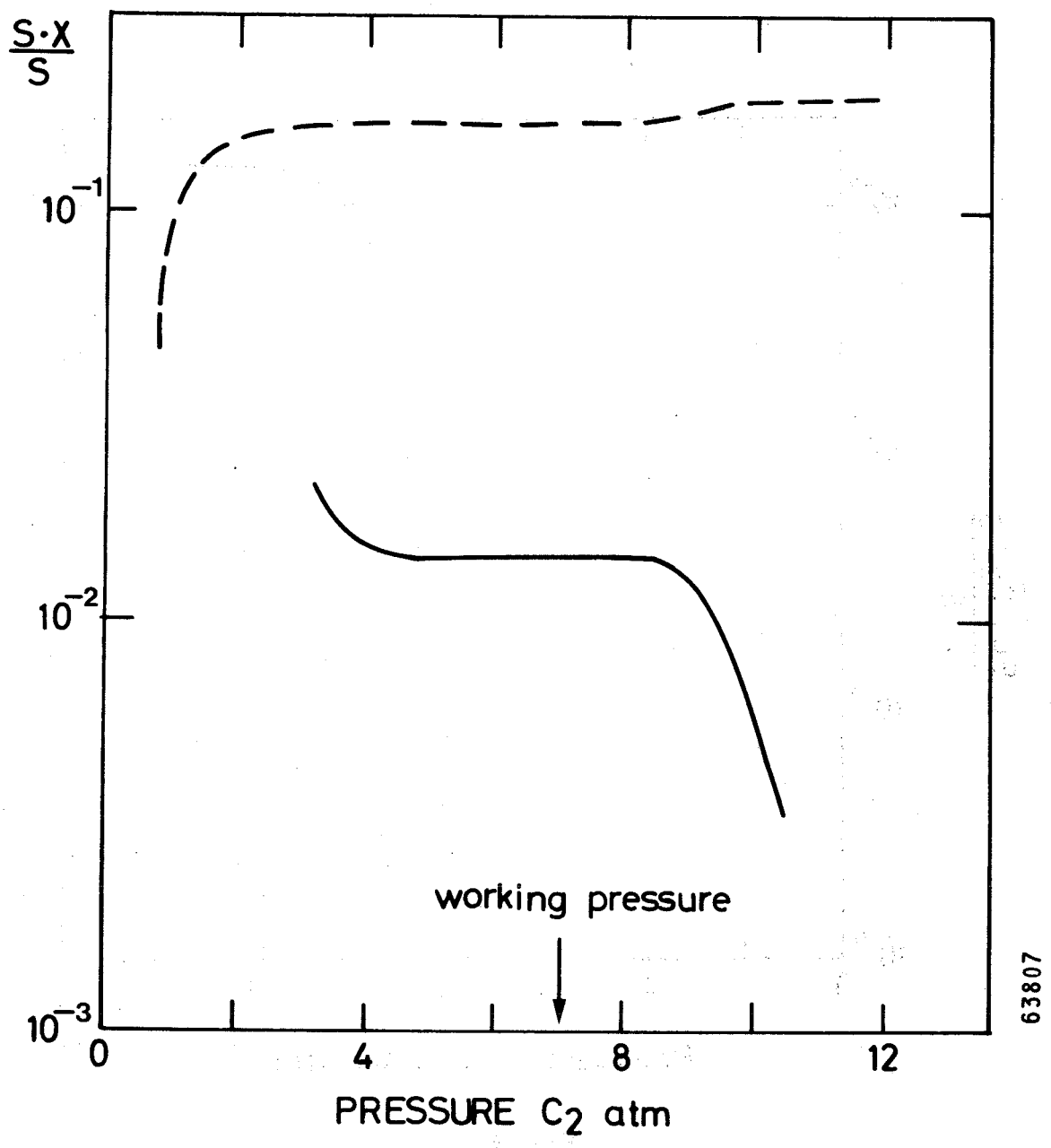
S·X
S
10^{-1}
10^{-2}
10^{-3}
working pressure
0
4
8
12
PRESSURE C_2 atm
63807

Fig. 3

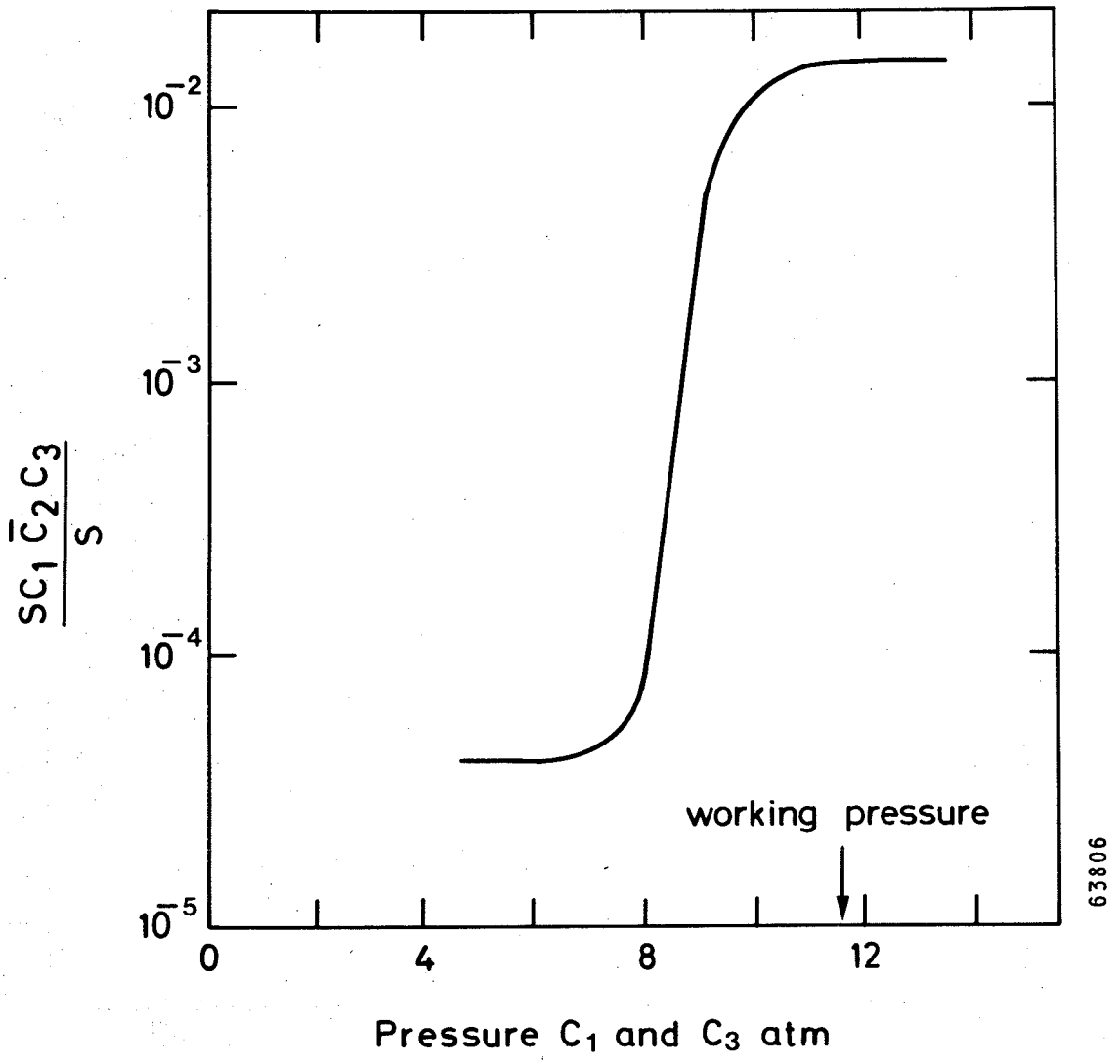
$\frac{SC_1\bar{C}_2C_3}{S}$
10^{-2}
10^{-3}
10^{-4}
10^{-5}
working pressure
63806
0
4
8
12
Pressure C_1 and C_3 atm

Fig. 4

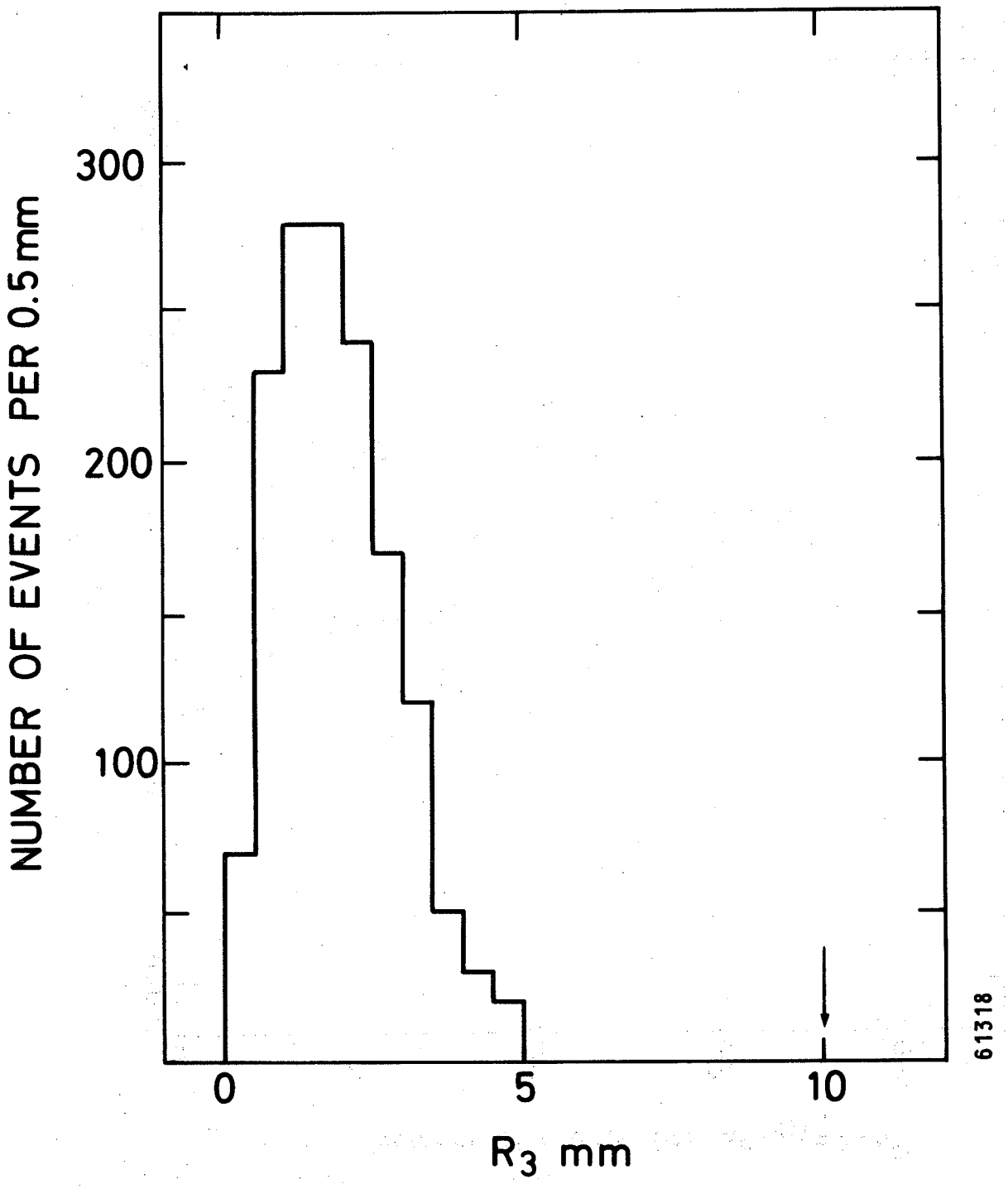

Fig. 5

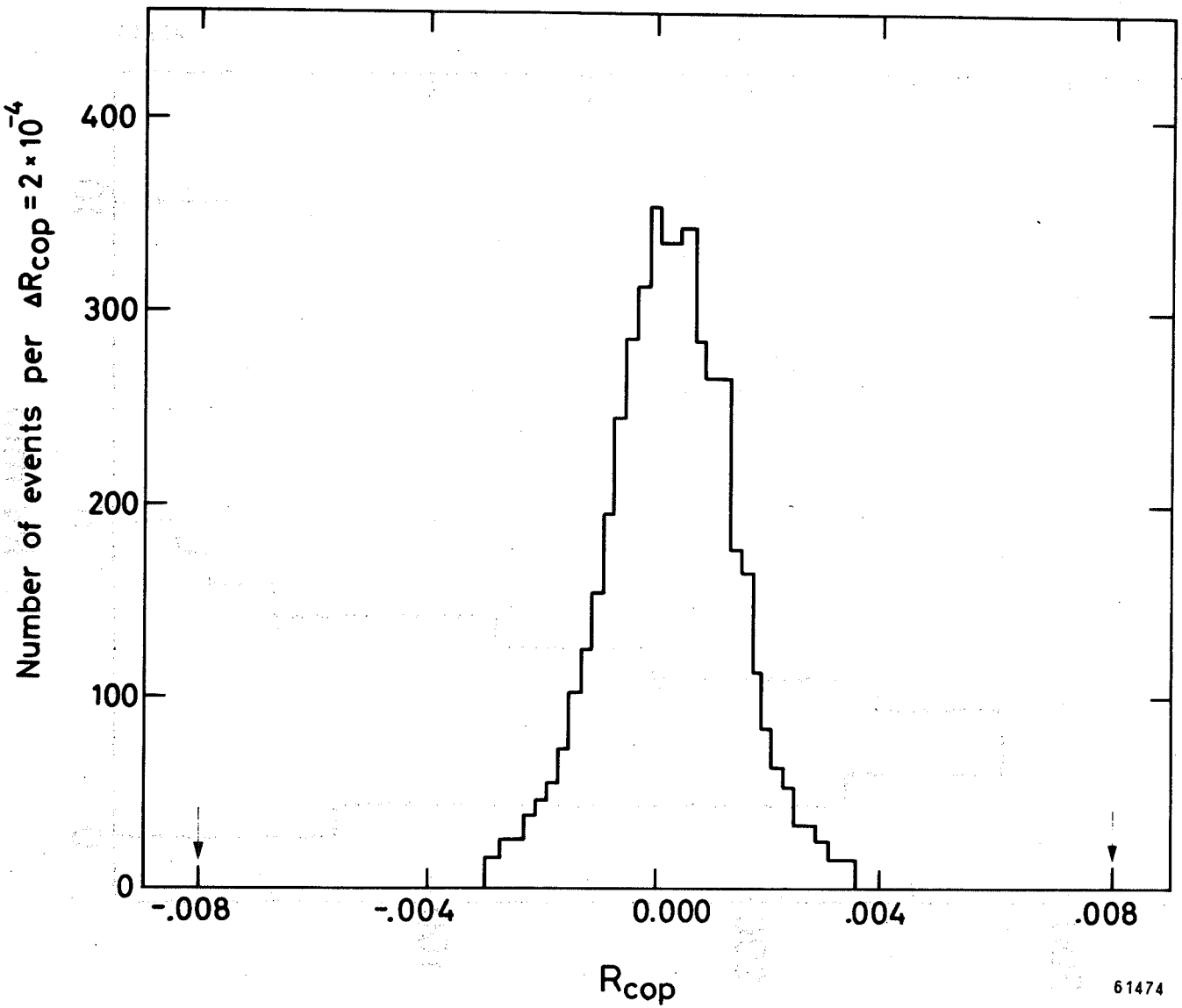
Number of events per $\Delta R_{cop} = 2 \times 10^{-4}$
400
300
200
100
0
-.008
-.004
0.000
.004
.008
R_{cop}
61474

Fig. 6

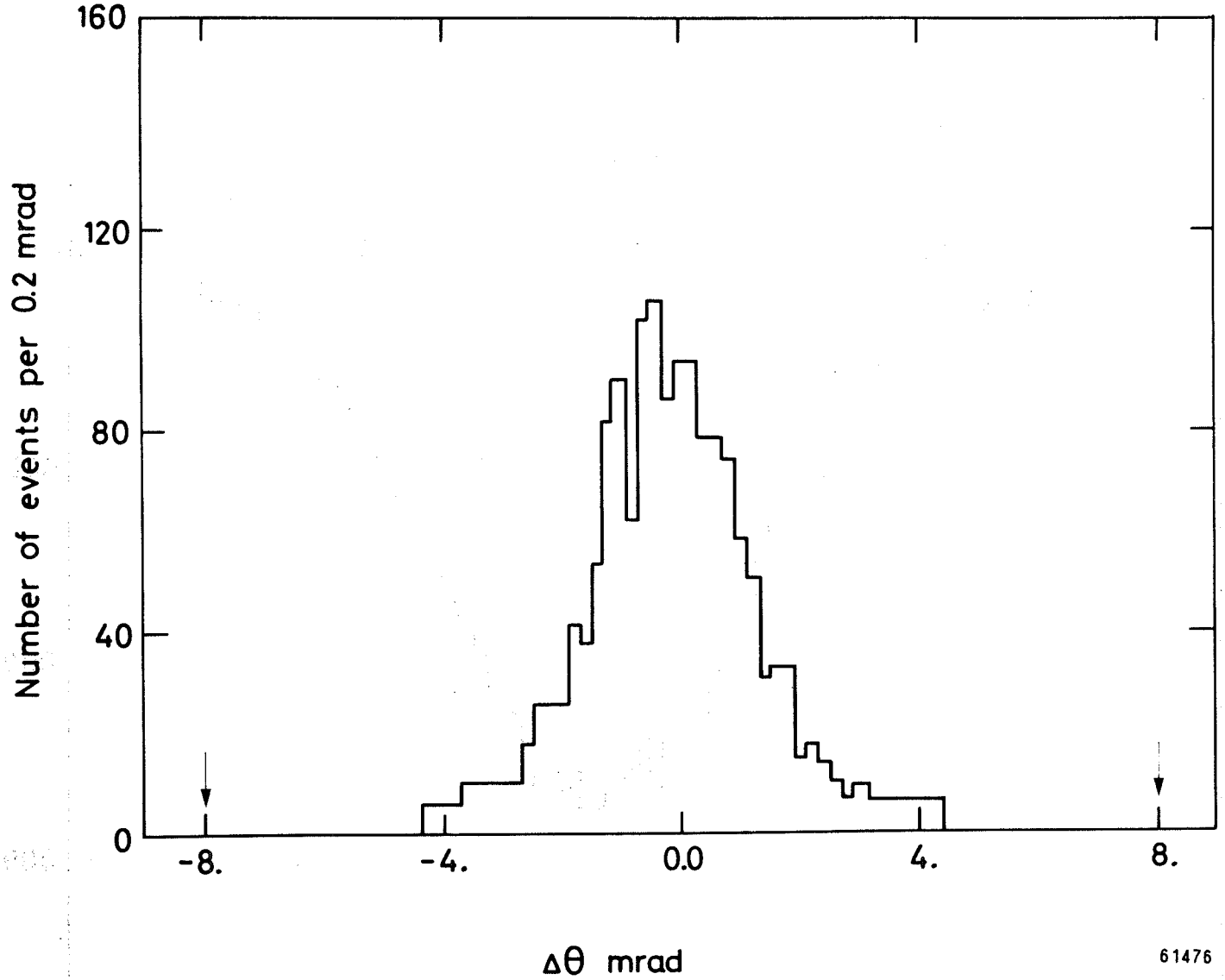
160
120
80
40
0
Number of events per 0.2 mrad
-8.
-4.
0.0
4.
8.
Δθ mrad
61476

Fig. 7

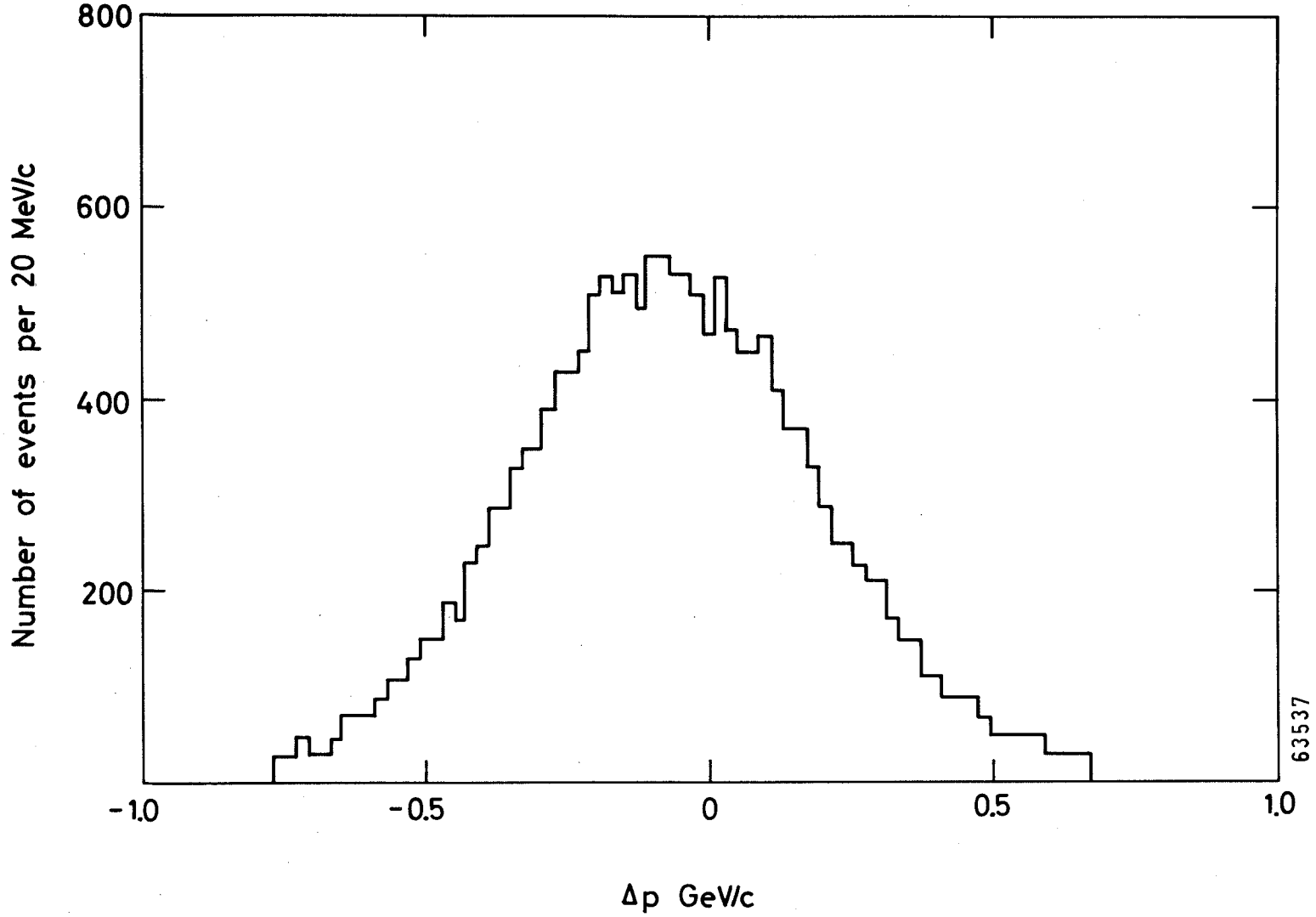
800
600
400
200
Number of events per 20 MeV/c
-1.0
-0.5
0
0.5
1.0
Δp GeV/c
63537

Fig. 8

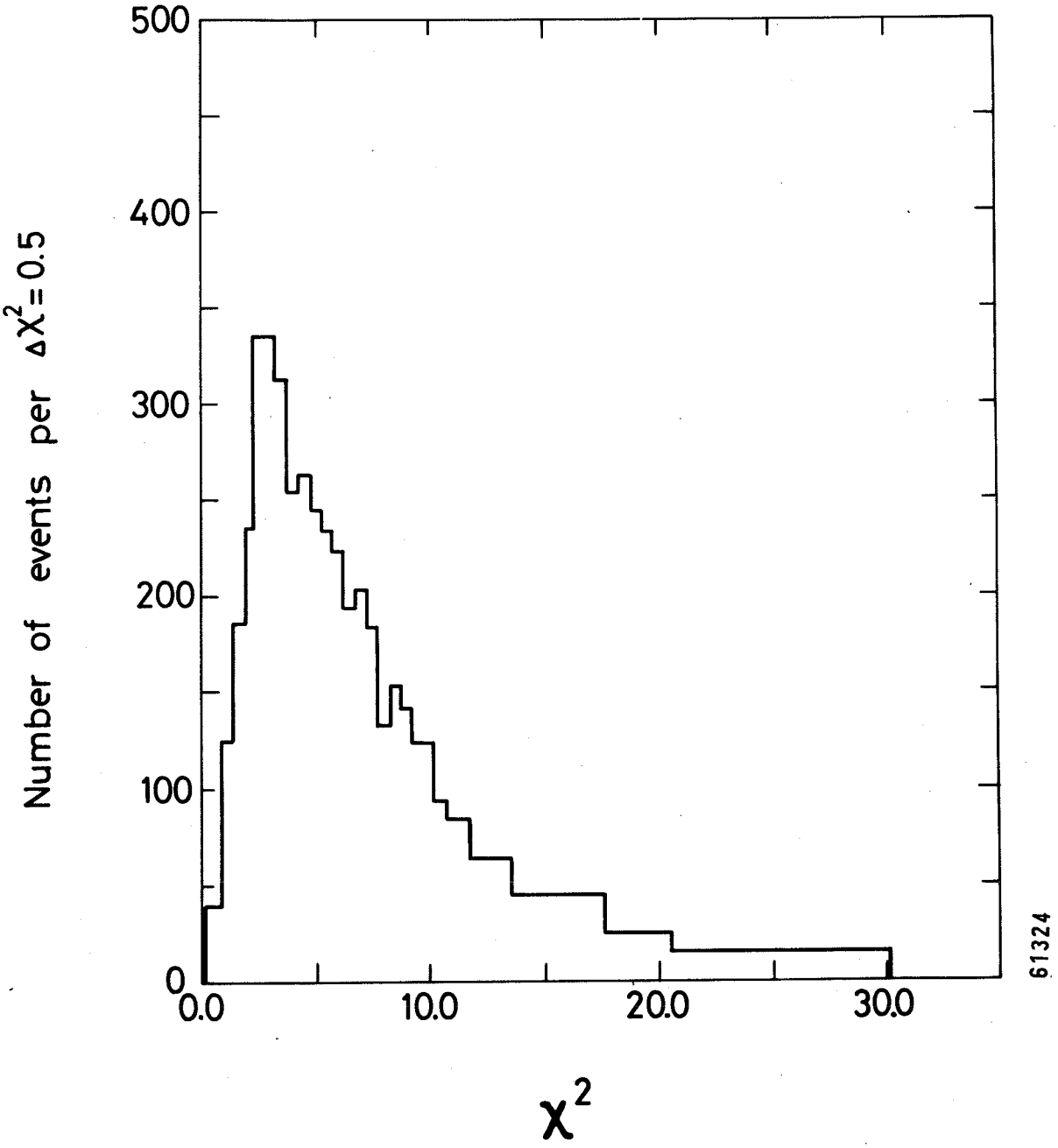
500
400
300
200
100
0
0.0
10.0
20.0
30.0
Number of events per $\Delta\chi^2 = 0.5$
χ^2
61324

Fig. 9

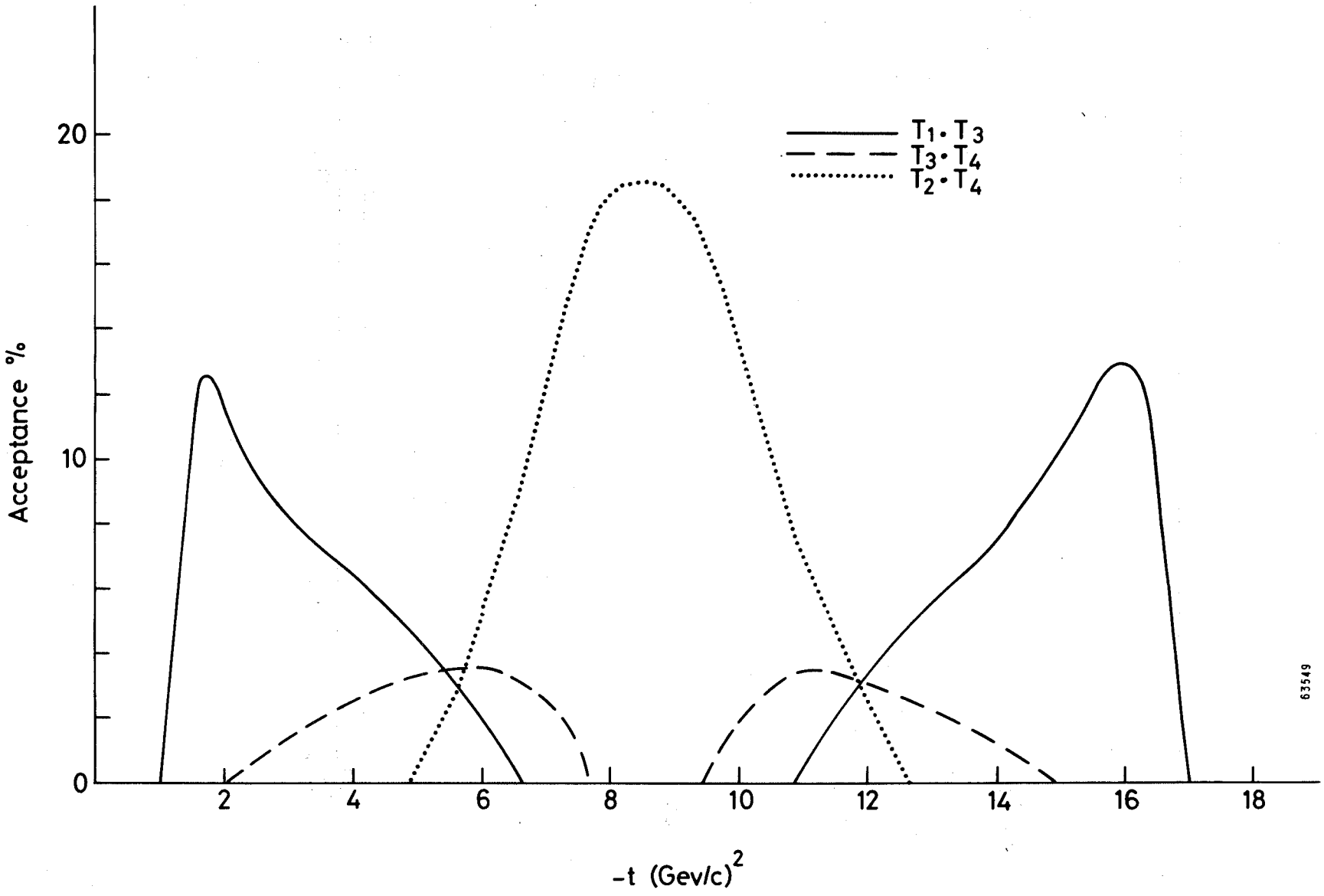
20
10
0
Acceptance %
$T_1 \cdot T_3$
$T_3 \cdot T_4$
$T_2 \cdot T_4$
2
4
6
8
10
12
14
16
18
$-t\ (Gev/c)^2$
63549

Fig. 10

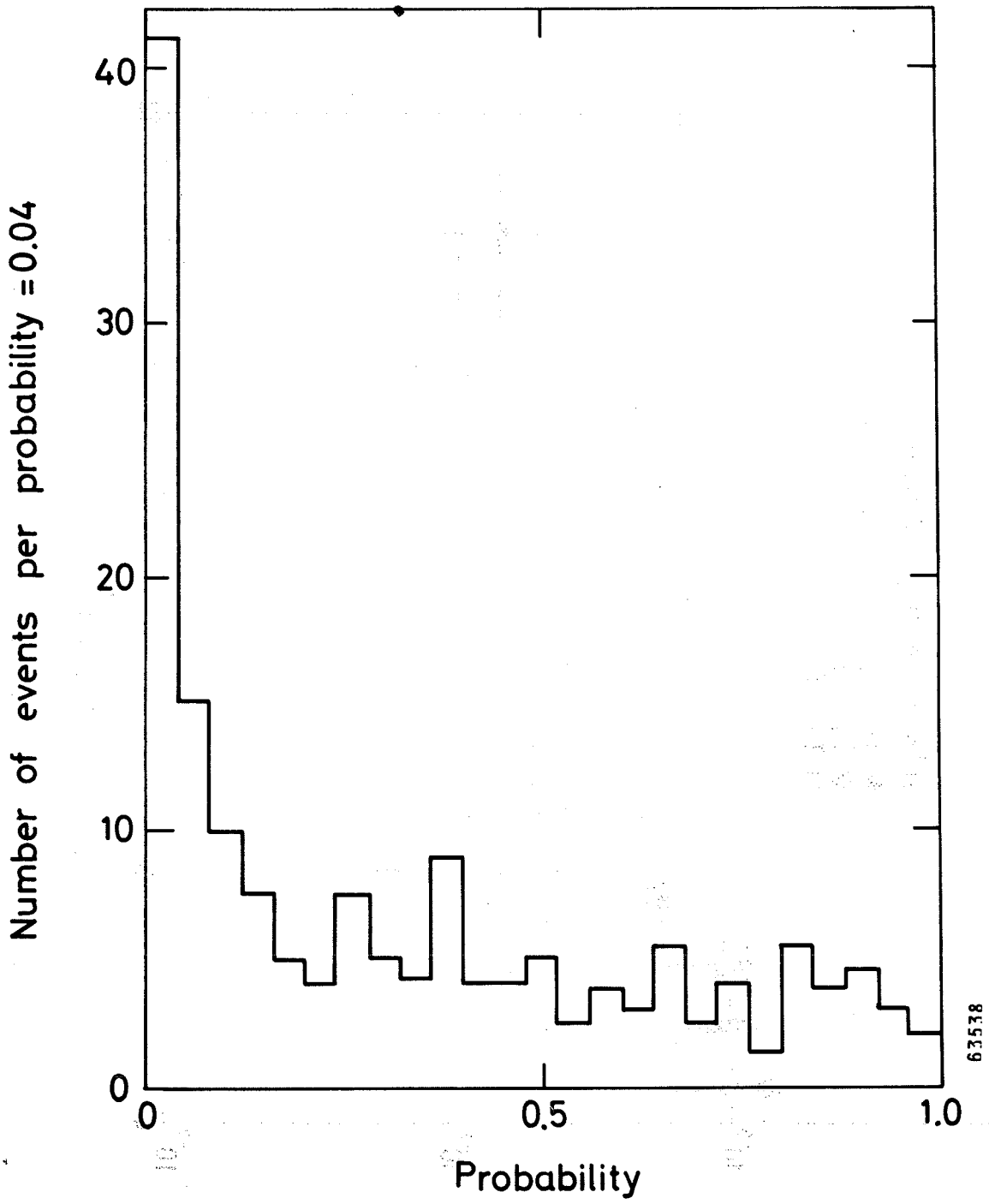
Number of events per probability = 0.04
40
30
20
10
0
0
0.5
1.0
Probability
63538

Fig. 11

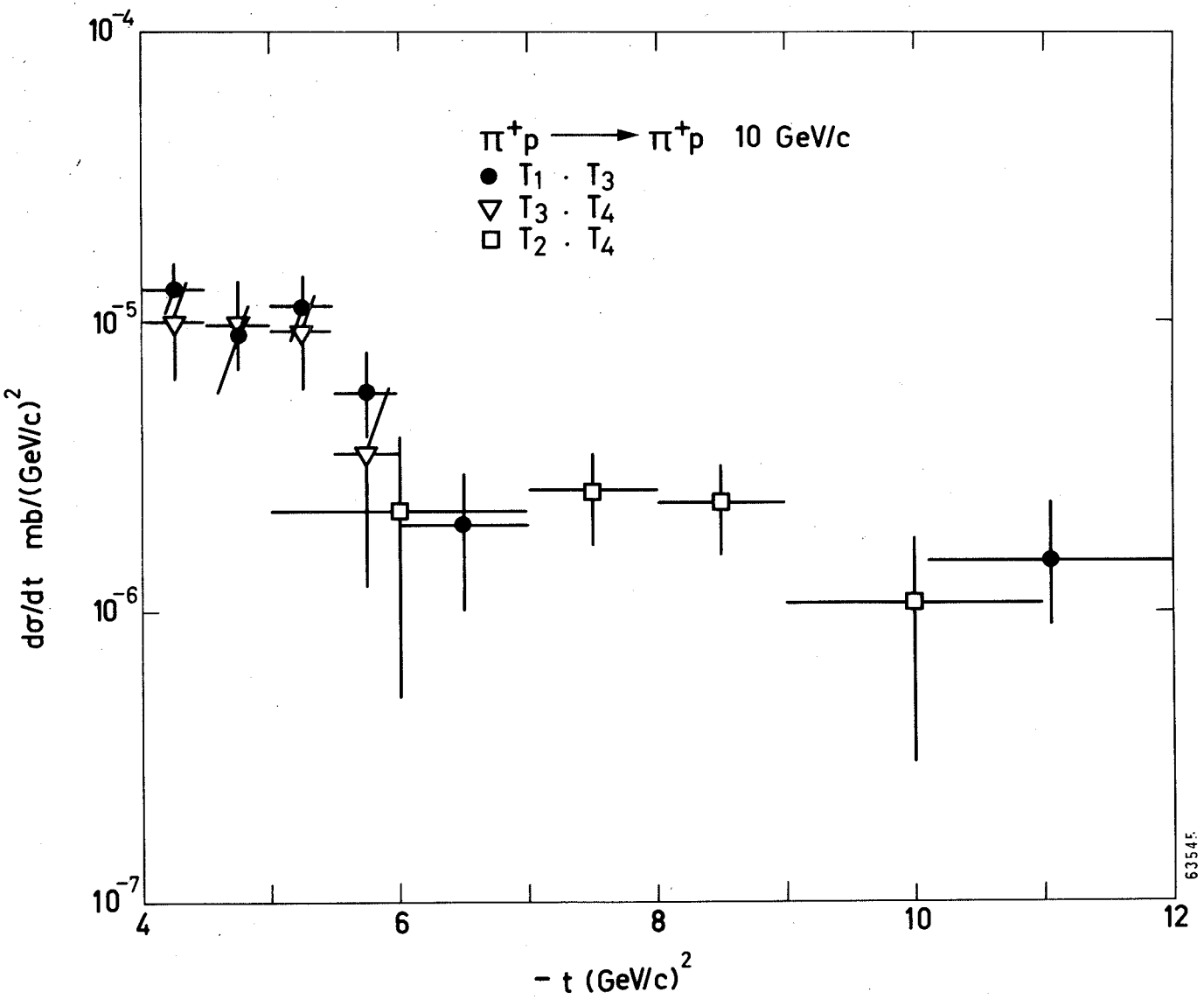
10^{-4}
10^{-5}
10^{-6}
10^{-7}
$\pi^+p \longrightarrow \pi^+p$ 10 GeV/c
● $T_1 \cdot T_3$
▽ $T_3 \cdot T_4$
□ $T_2 \cdot T_4$
$d\sigma/dt$ mb/(GeV/c)^2
4
6
8
10
12
$-t$ (GeV/c)^2
63545

Fig. 12

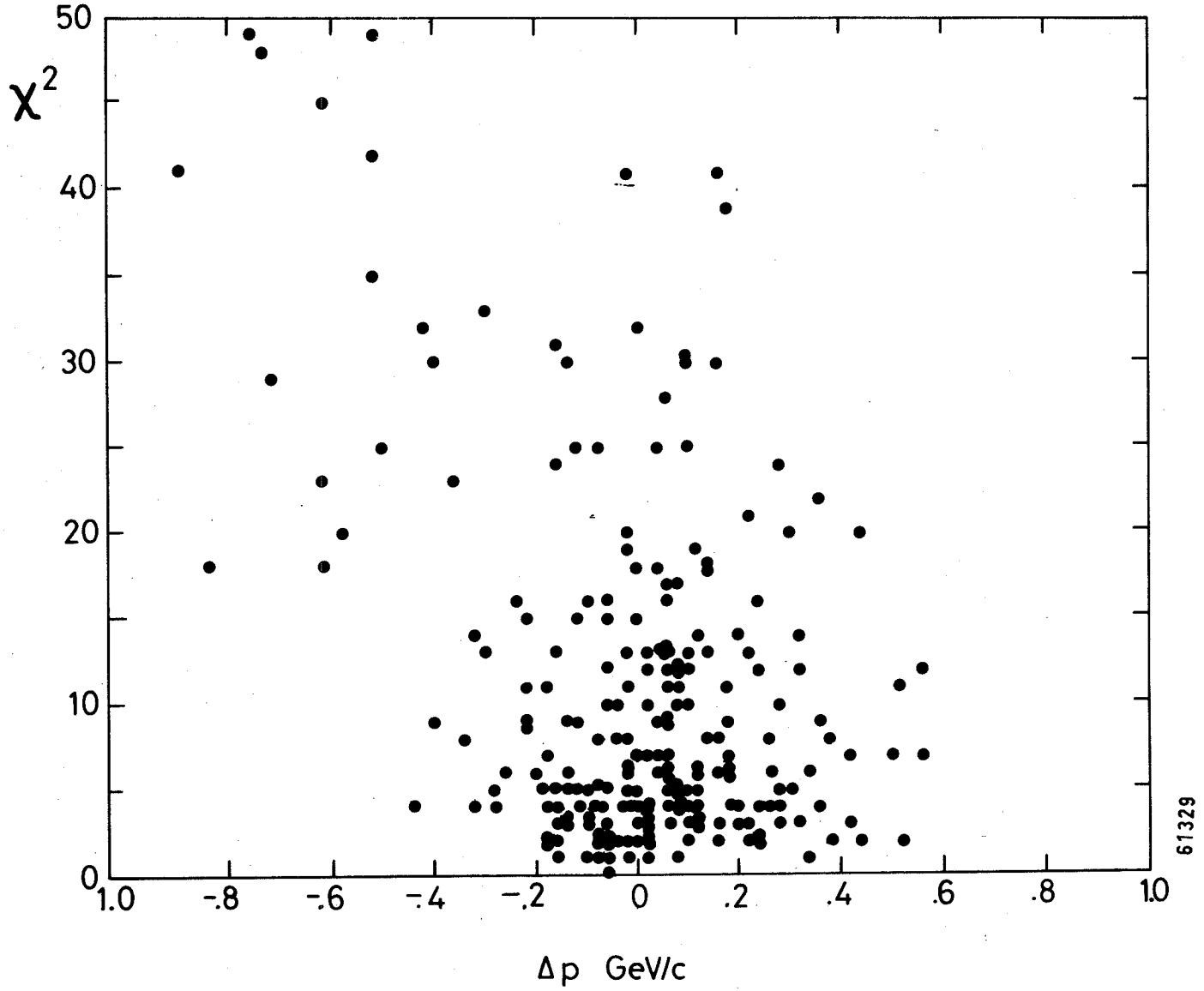

Fig. 13

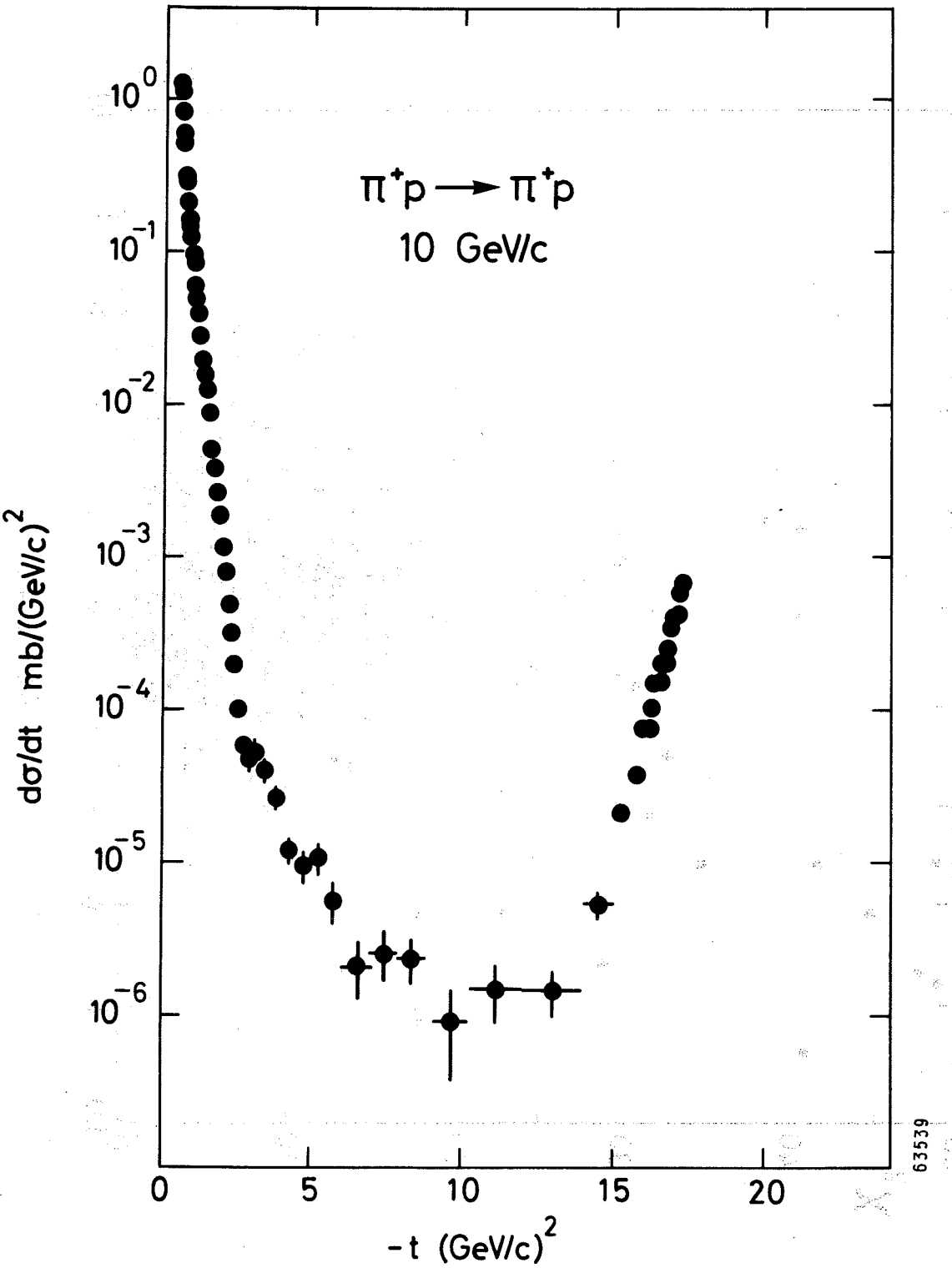
$\pi^+p \longrightarrow \pi^+p$
10 GeV/c
$d\sigma/dt$ mb/(GeV/c)^2
10^0
10^{-1}
10^{-2}
10^{-3}
10^{-4}
10^{-5}
10^{-6}
0
5
10
15
20
$-t$ (GeV/c)^2
63539

Fig. 14

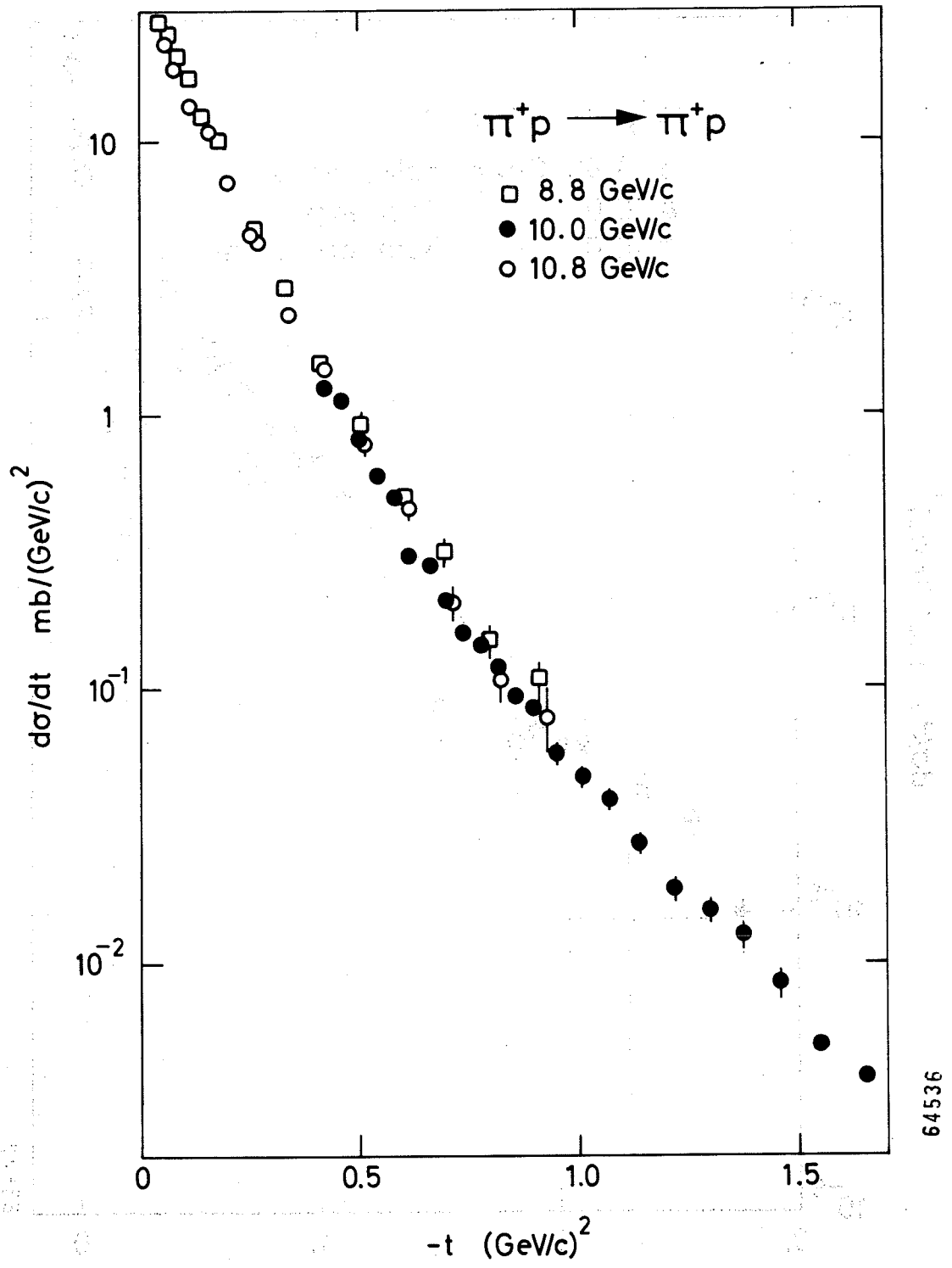
$\pi^+p \longrightarrow \pi^+p$
8.8 GeV/c
10.0 GeV/c
10.8 GeV/c
10
1
10^{-1}
10^{-2}
$d\sigma/dt$ mb/(GeV/c)^2
0
0.5
1.0
1.5
-t (GeV/c)^2
64536

Fig. 15

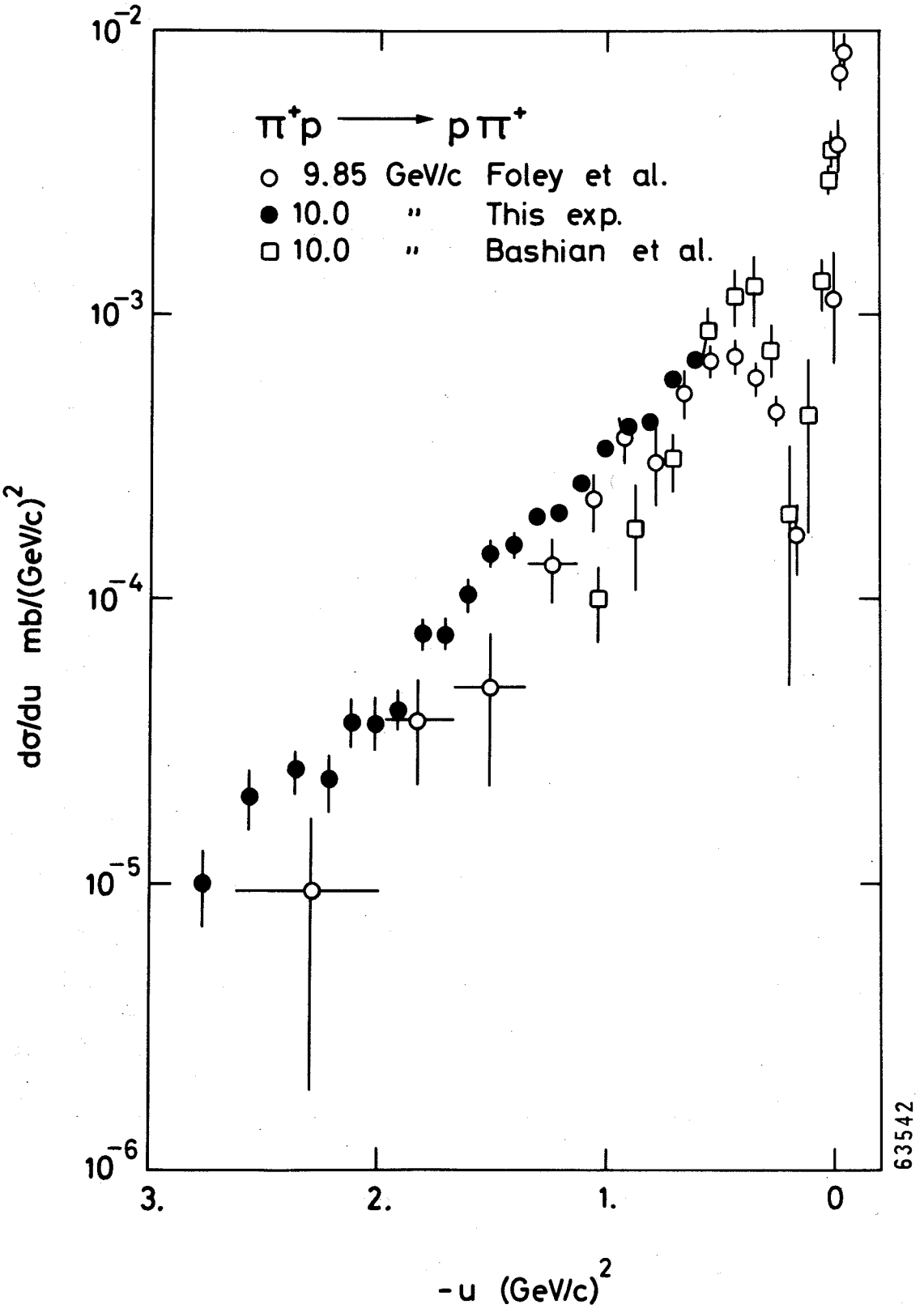
$\pi^+p \longrightarrow p\pi^+$
○ 9.85 GeV/c Foley et al.
● 10.0 " This exp.
□ 10.0 " Bashian et al.
10^{-2}
10^{-3}
10^{-4}
10^{-5}
10^{-6}
$d\sigma/du$ mb/(GeV/c)^2
3.
2.
1.
0
$-u$ (GeV/c)^2
63542

Fig. 16

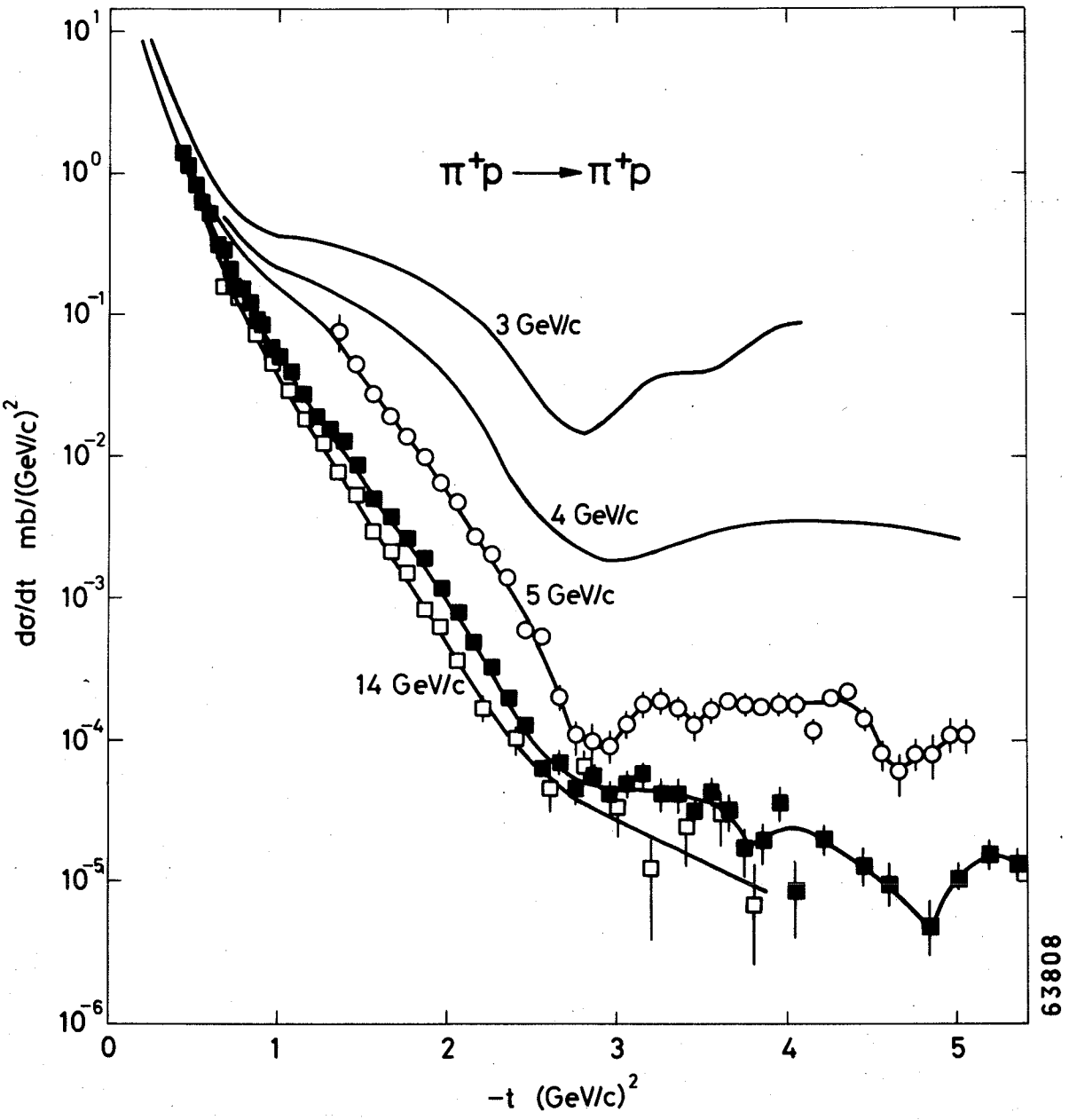
$\pi^+p \longrightarrow \pi^+p$
3 GeV/c
4 GeV/c
5 GeV/c
14 GeV/c
$d\sigma/dt$ mb/(GeV/c)^2
$-t$ (GeV/c)^2
63808

Fig. 17

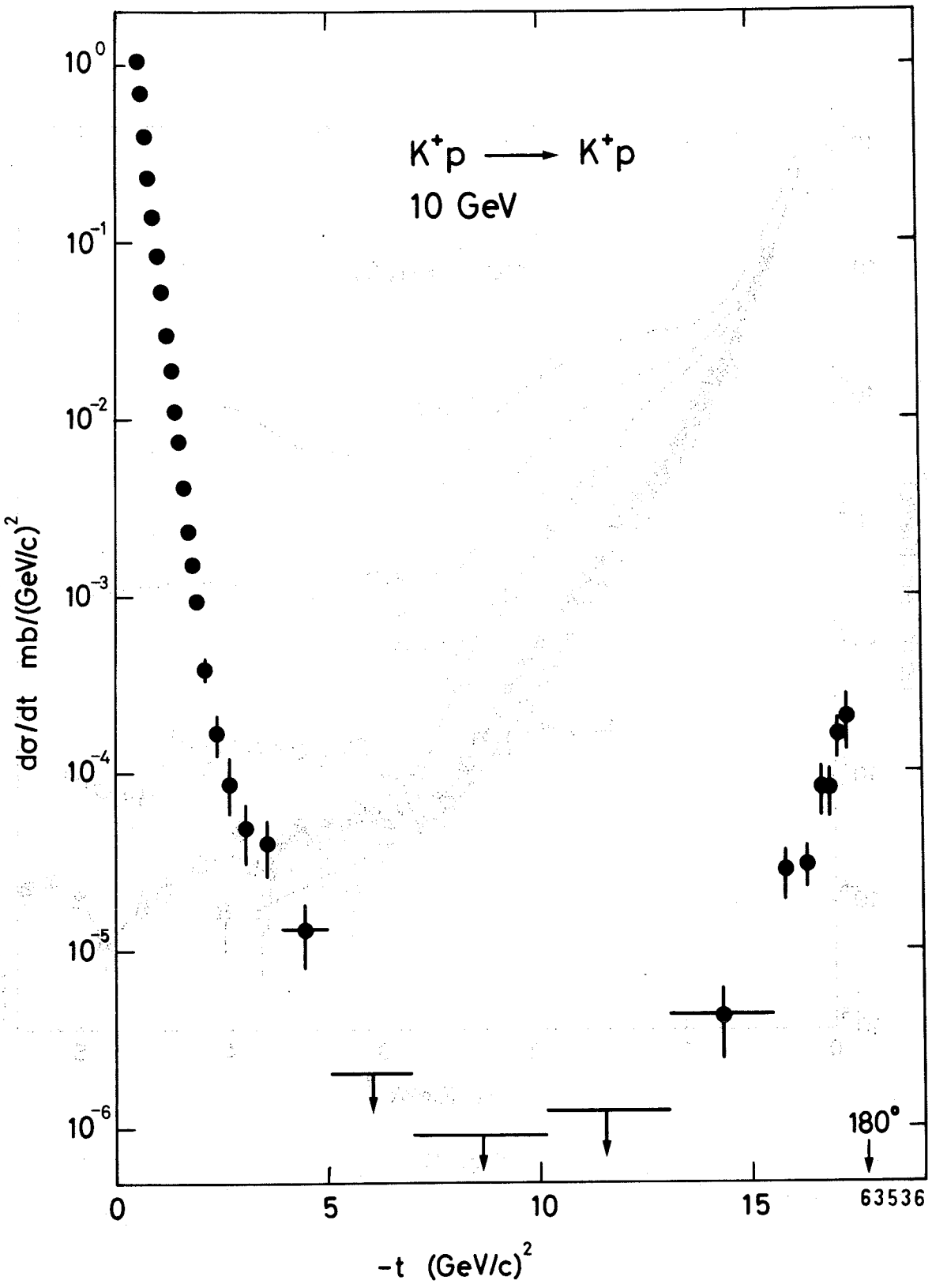
$K^+p \longrightarrow K^+p$
10 GeV
10^0
10^{-1}
10^{-2}
10^{-3}
10^{-4}
10^{-5}
10^{-6}
$d\sigma/dt$ mb/(GeV/c)^2
0
5
10
15
$-t$ (GeV/c)^2
180°
63536

Fig. 18

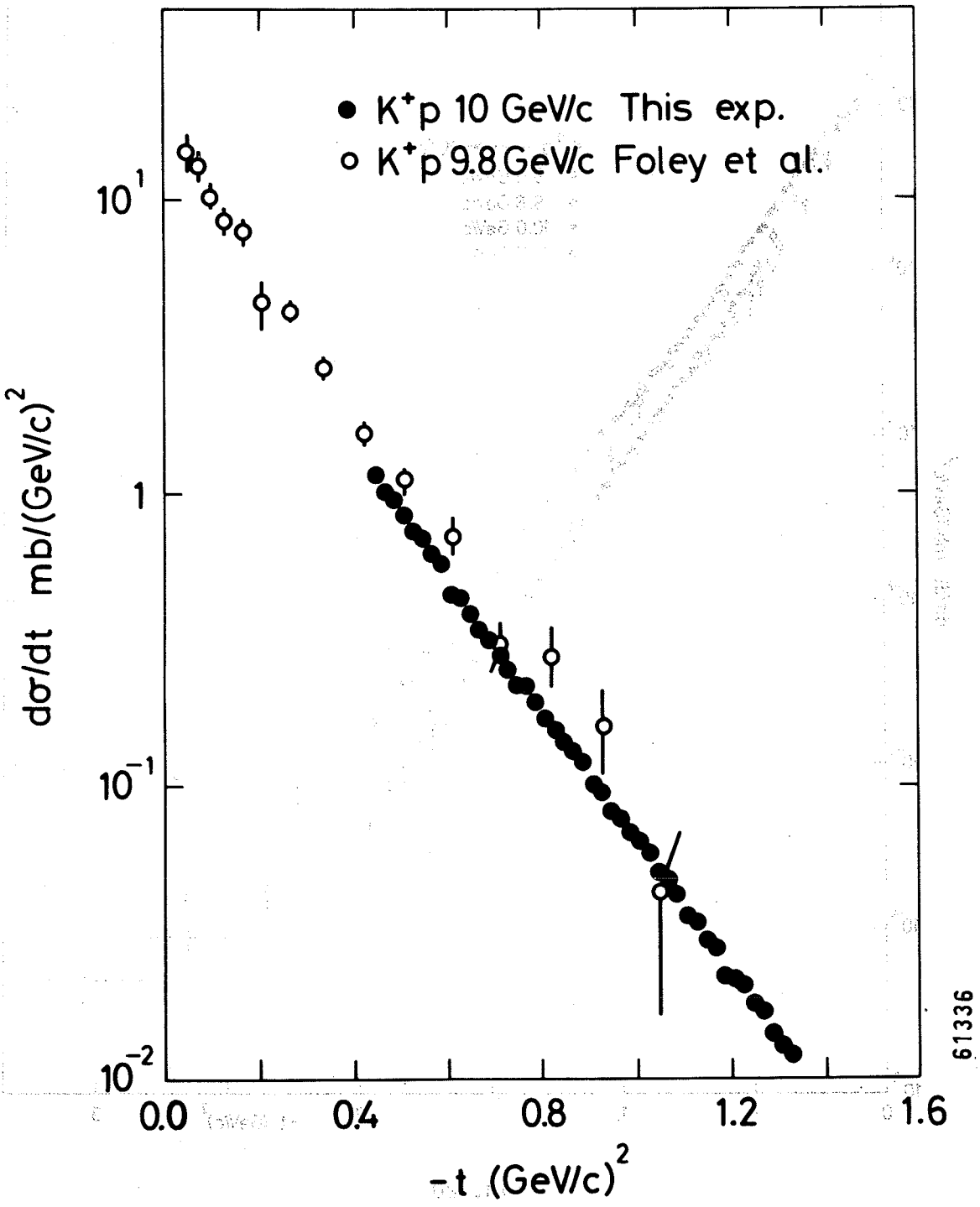
● K⁺p 10 GeV/c This exp.
○ K⁺p 9.8 GeV/c Foley et al.
dσ/dt mb/(GeV/c)²
10¹
1
10⁻¹
10⁻²
0.0
0.4
0.8
1.2
1.6
-t (GeV/c)²
61336

Fig. 19

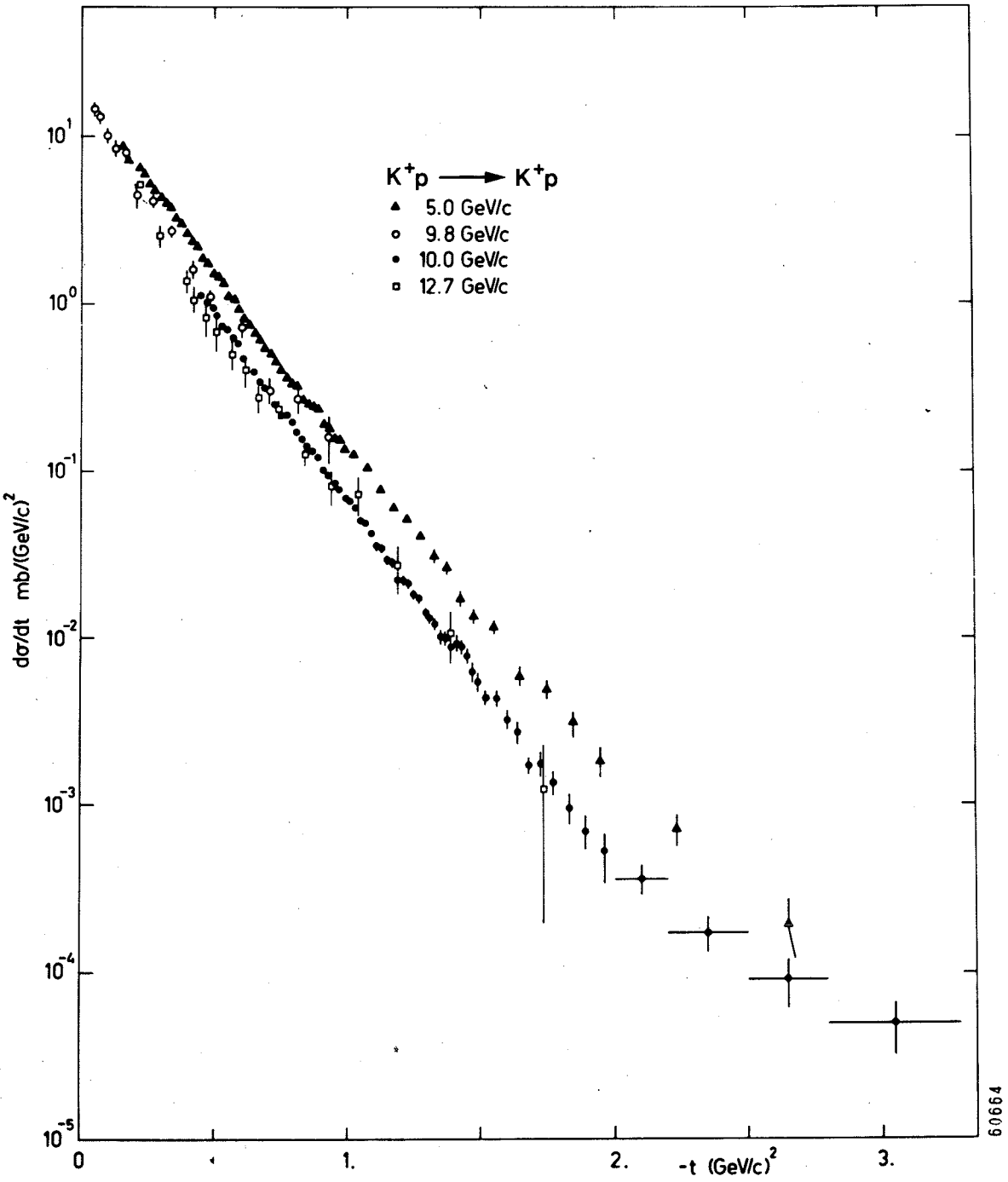
$K^+p \longrightarrow K^+p$
5.0 GeV/c
9.8 GeV/c
10.0 GeV/c
12.7 GeV/c
$d\sigma/dt$ mb/(GeV/c)^2
10^1
10^0
10^{-1}
10^{-2}
10^{-3}
10^{-4}
10^{-5}
0
1.
2.
3.
-t (GeV/c)^2
60664

Fig. 20

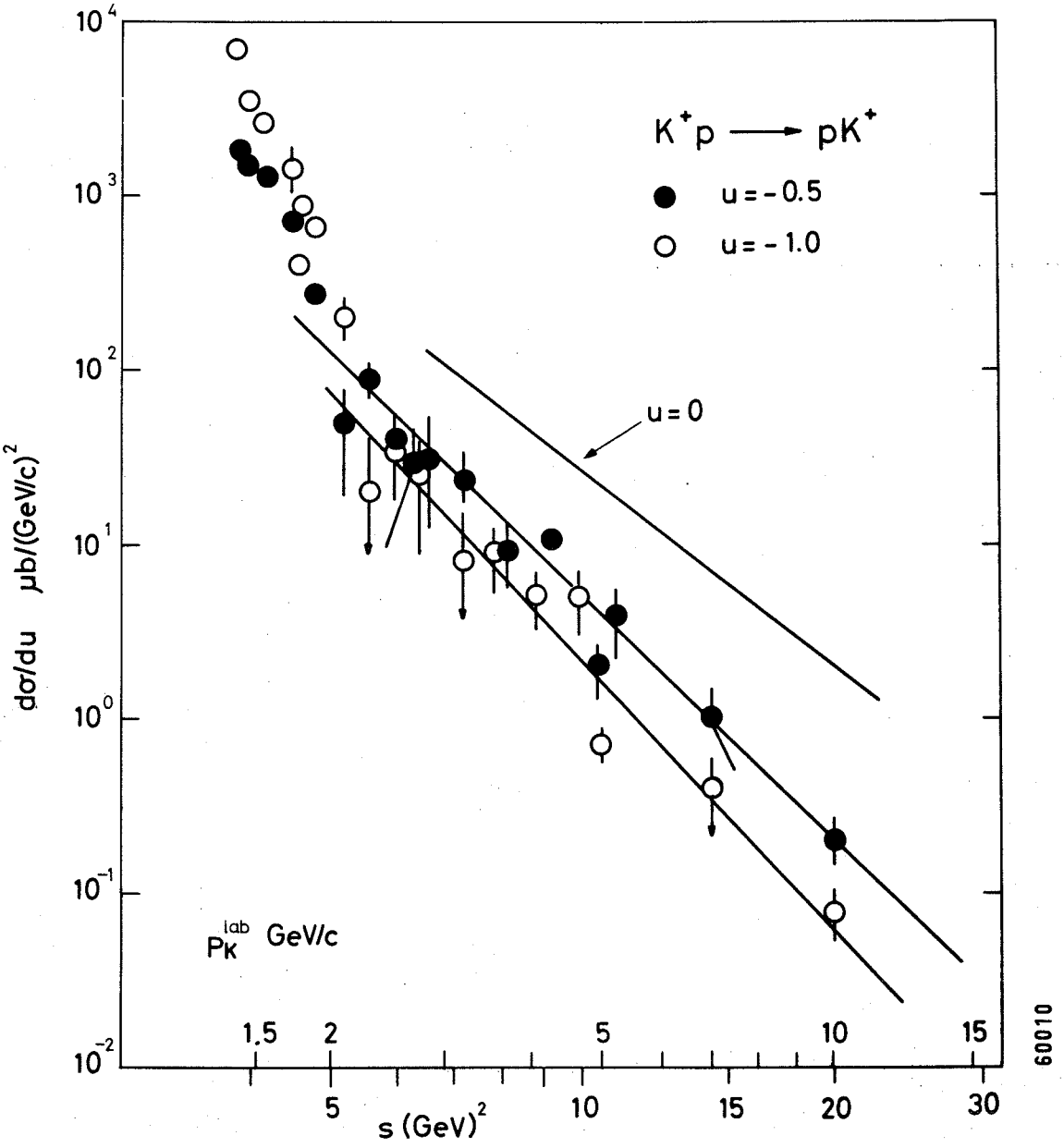
$K^+p \longrightarrow pK^+$
u = -0.5
u = -1.0
u = 0
$d\sigma/du$ μb/(GeV/c)^2
P_K^{lab} GeV/c
1.5
2
5
10
15
s (GeV)^2
5
10
15
20
30
60010

Fig. 21

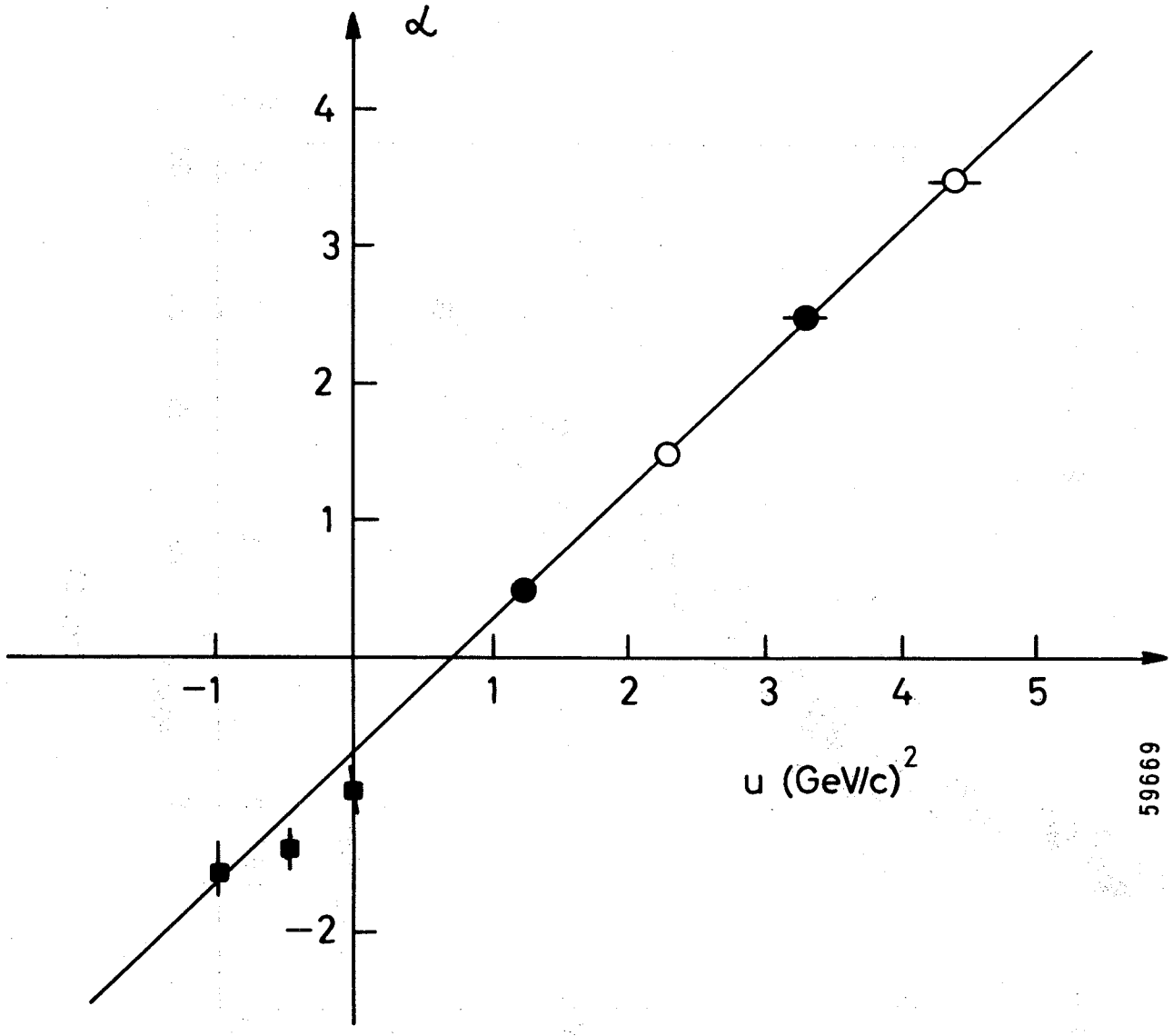

Fig. 22

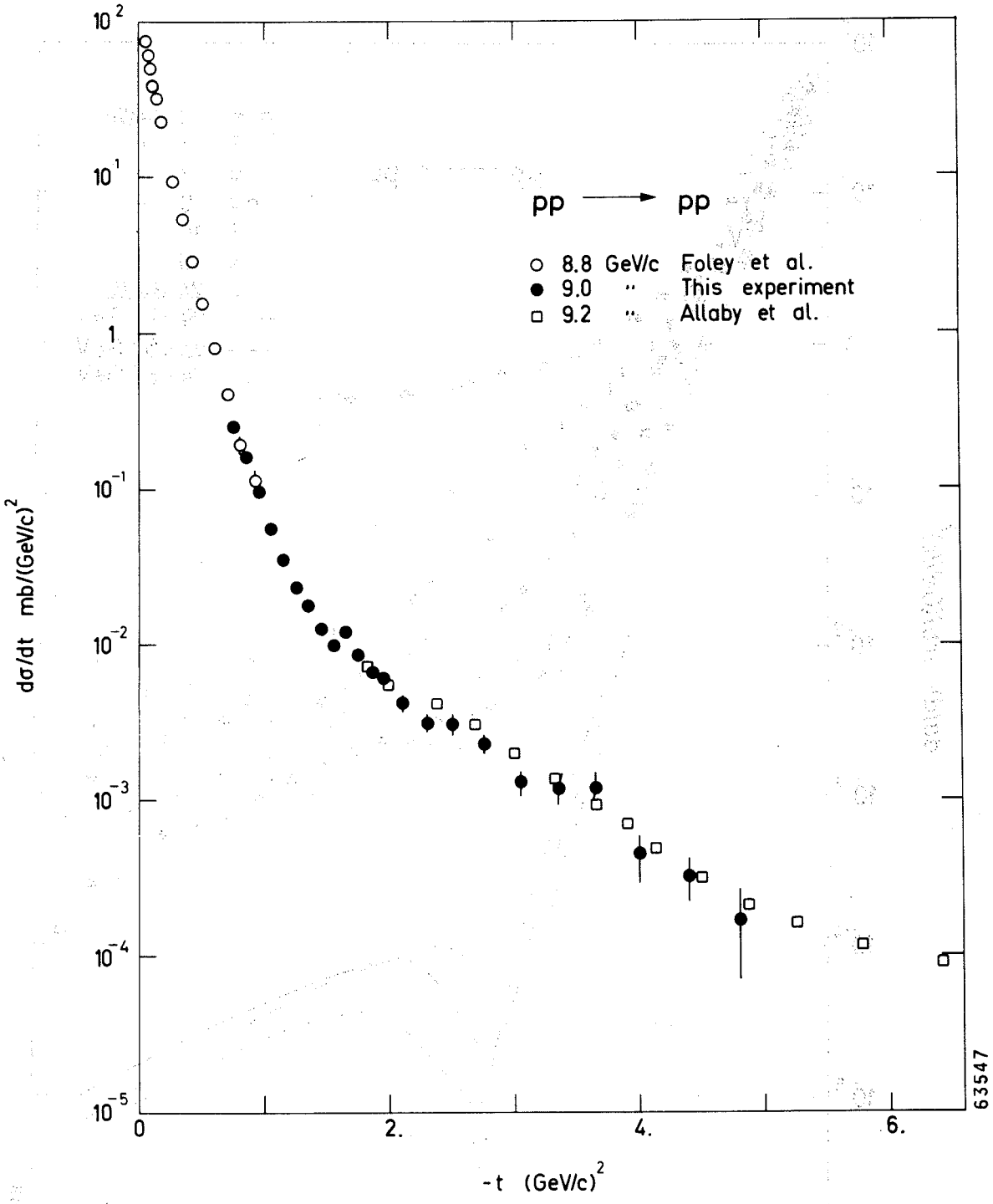
pp ⟶ pp
8.8 GeV/c Foley et al.
9.0 " This experiment
9.2 " Allaby et al.
dσ/dt mb/(GeV/c)²
-t (GeV/c)²
63547

Fig. 23

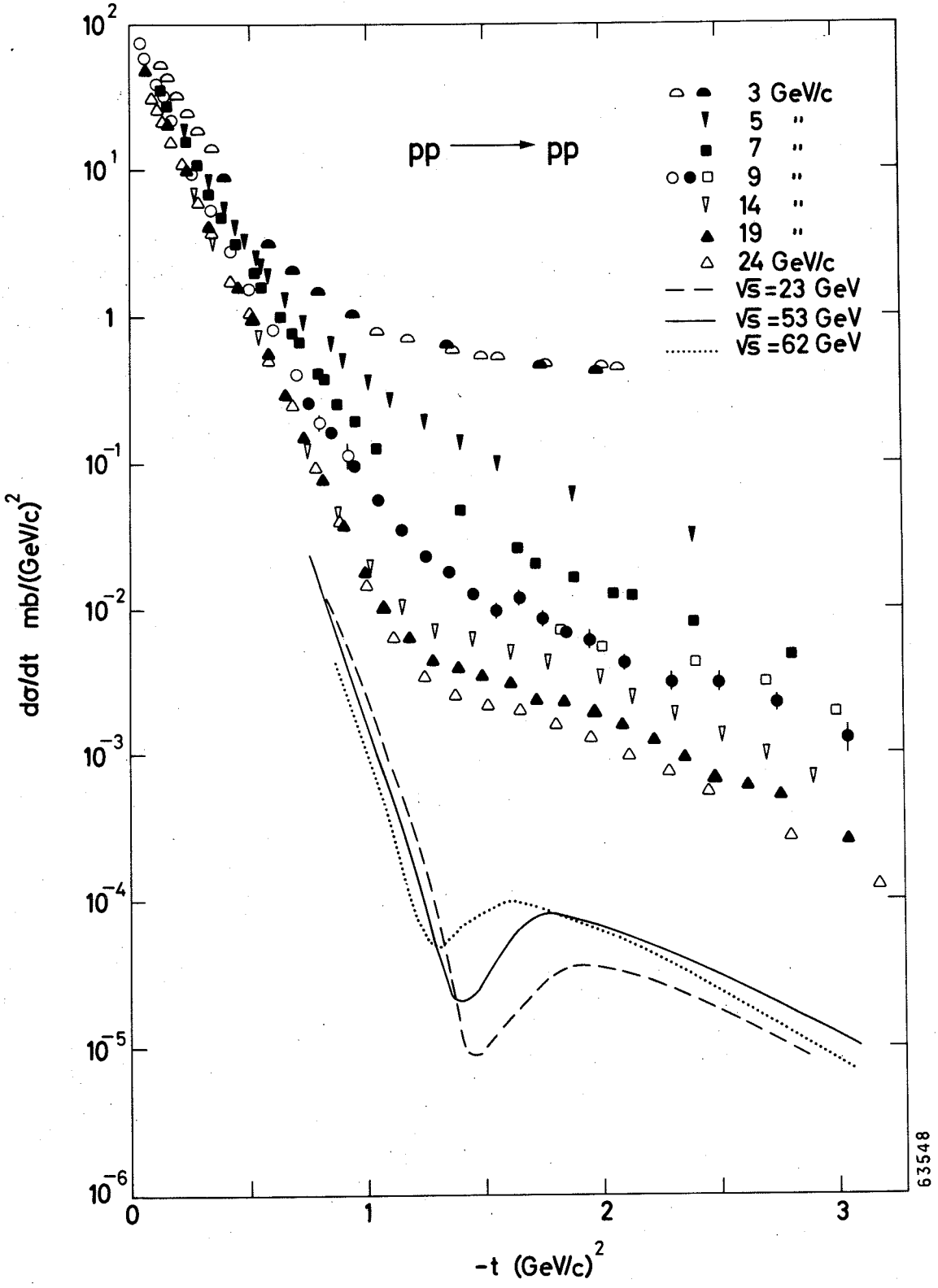
pp → pp
3 GeV/c
5 "
7 "
9 "
14 "
19 "
24 GeV/c
√s=23 GeV
√s=53 GeV
√s=62 GeV
dσ/dt mb/(GeV/c)²
-t (GeV/c)²
63548

Fig. 24

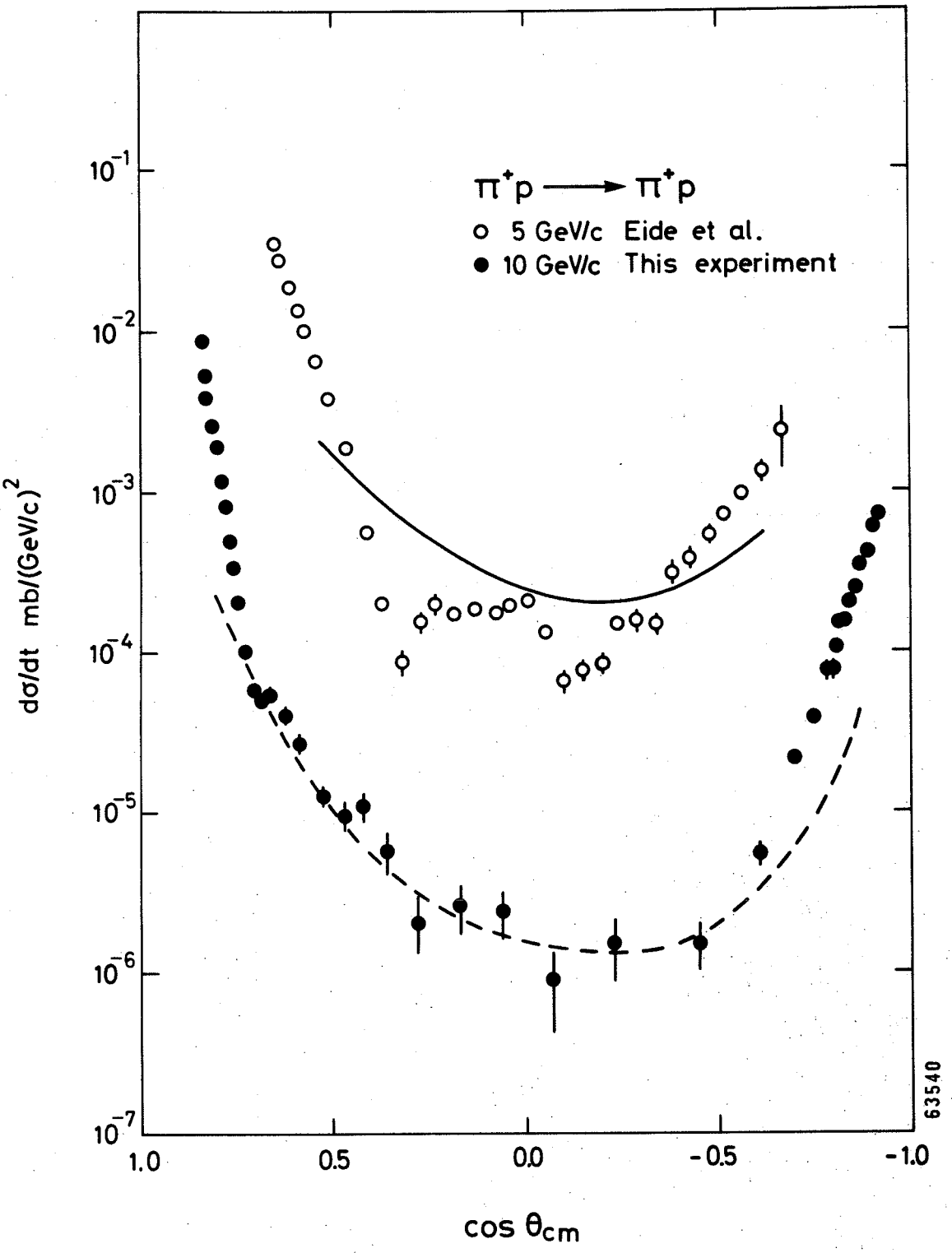
$\pi^+p \longrightarrow \pi^+p$
5 GeV/c Eide et al.
10 GeV/c This experiment
$d\sigma/dt$ mb/(GeV/c)^2
10^{-1}
10^{-2}
10^{-3}
10^{-4}
10^{-5}
10^{-6}
10^{-7}
1.0
0.5
0.0
-0.5
-1.0
cos θ_{cm}
63540

Fig. 25

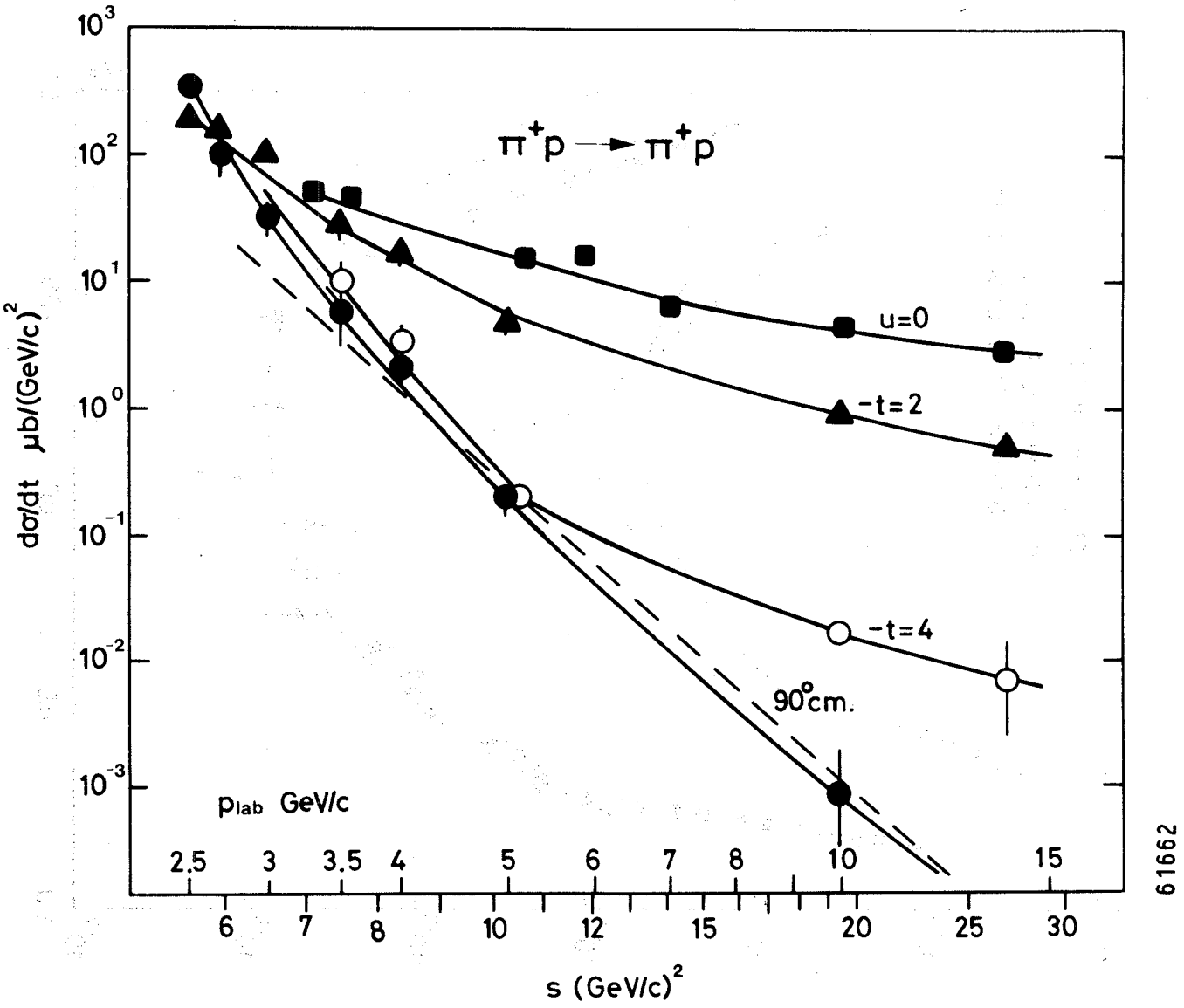
$\pi^+p \rightarrow \pi^+p$
u=0
-t=2
-t=4
90°cm.
$d\sigma/dt$ μb/(GeV/c)^2
p_{lab} GeV/c
2.5
3
3.5
4
5
6
7
8
10
15
6
7
8
10
12
15
20
25
30
s (GeV/c)^2
61662

Fig. 26

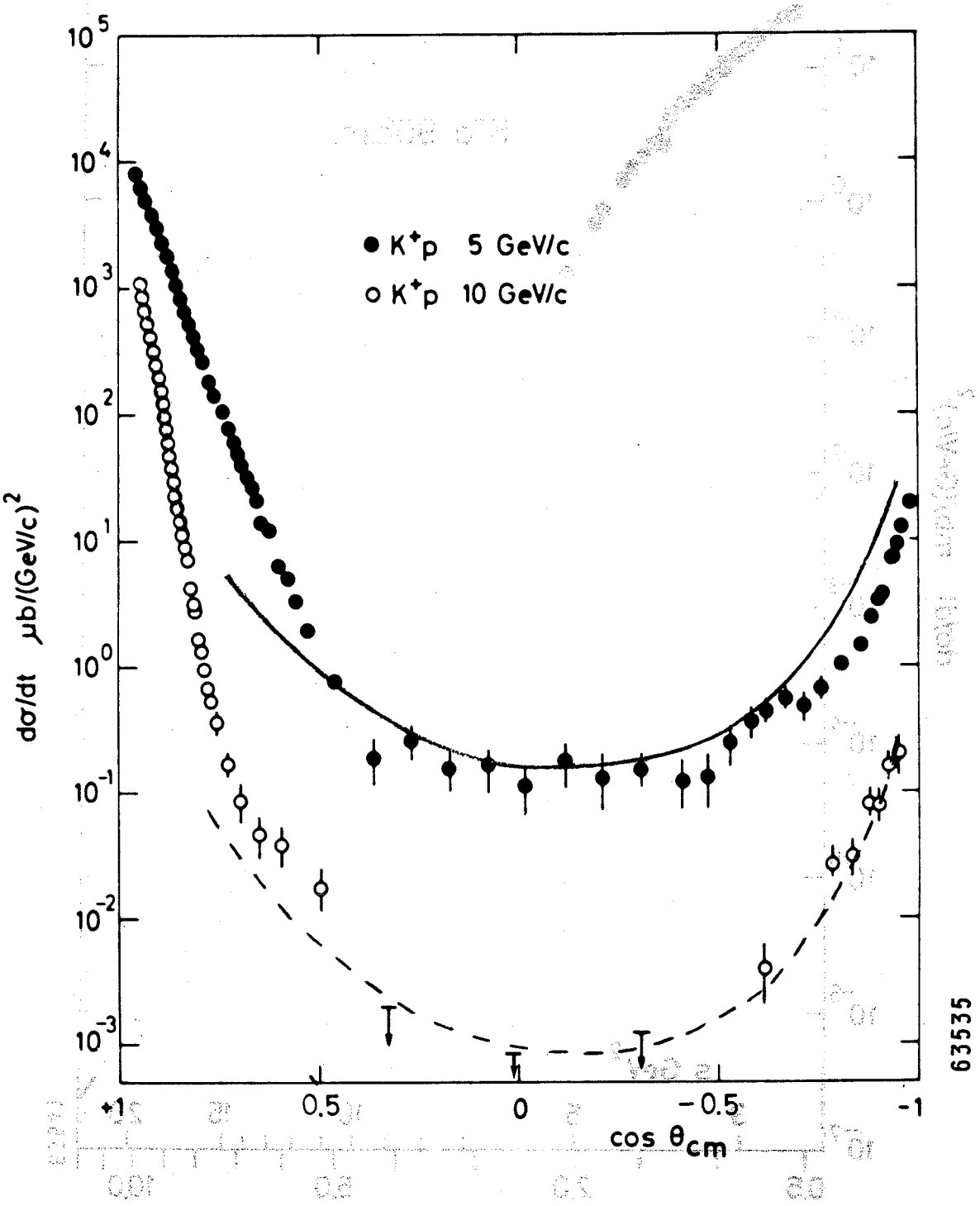
10^5
10^4
10^3
10^2
10^1
10^0
10^{-1}
10^{-2}
10^{-3}
● K⁺p 5 GeV/c
○ K⁺p 10 GeV/c
dσ/dt μb/(GeV/c)²
+1
0.5
0
−0.5
−1
cos θcm
63535

Fig. 27

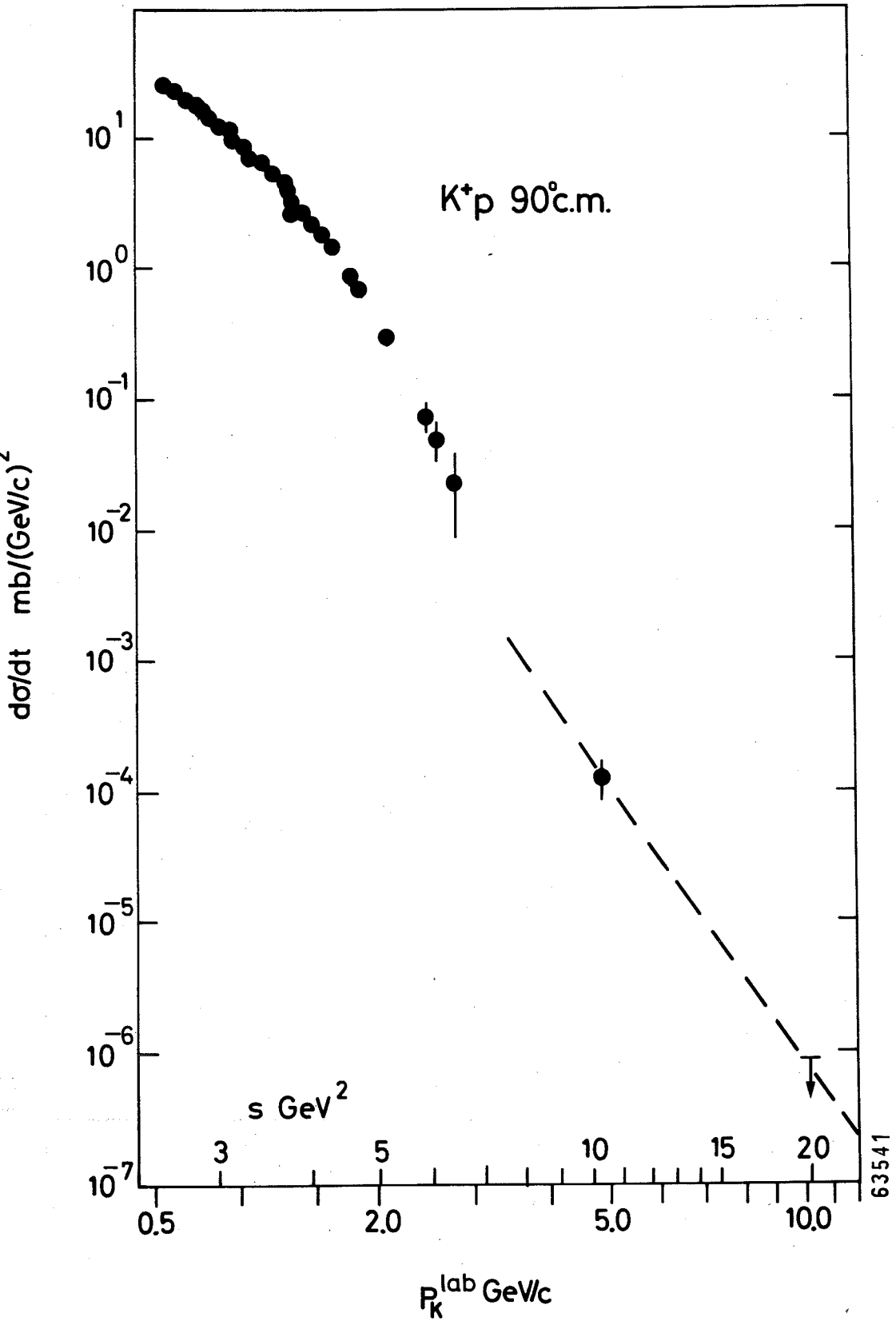
K⁺p 90°c.m.
dσ/dt mb/(GeV/c)²
10¹
10⁰
10⁻¹
10⁻²
10⁻³
10⁻⁴
10⁻⁵
10⁻⁶
10⁻⁷
s GeV²
3
5
10
15
20
0.5
2.0
5.0
10.0
P_K^lab GeV/c
63541

Fig. 28

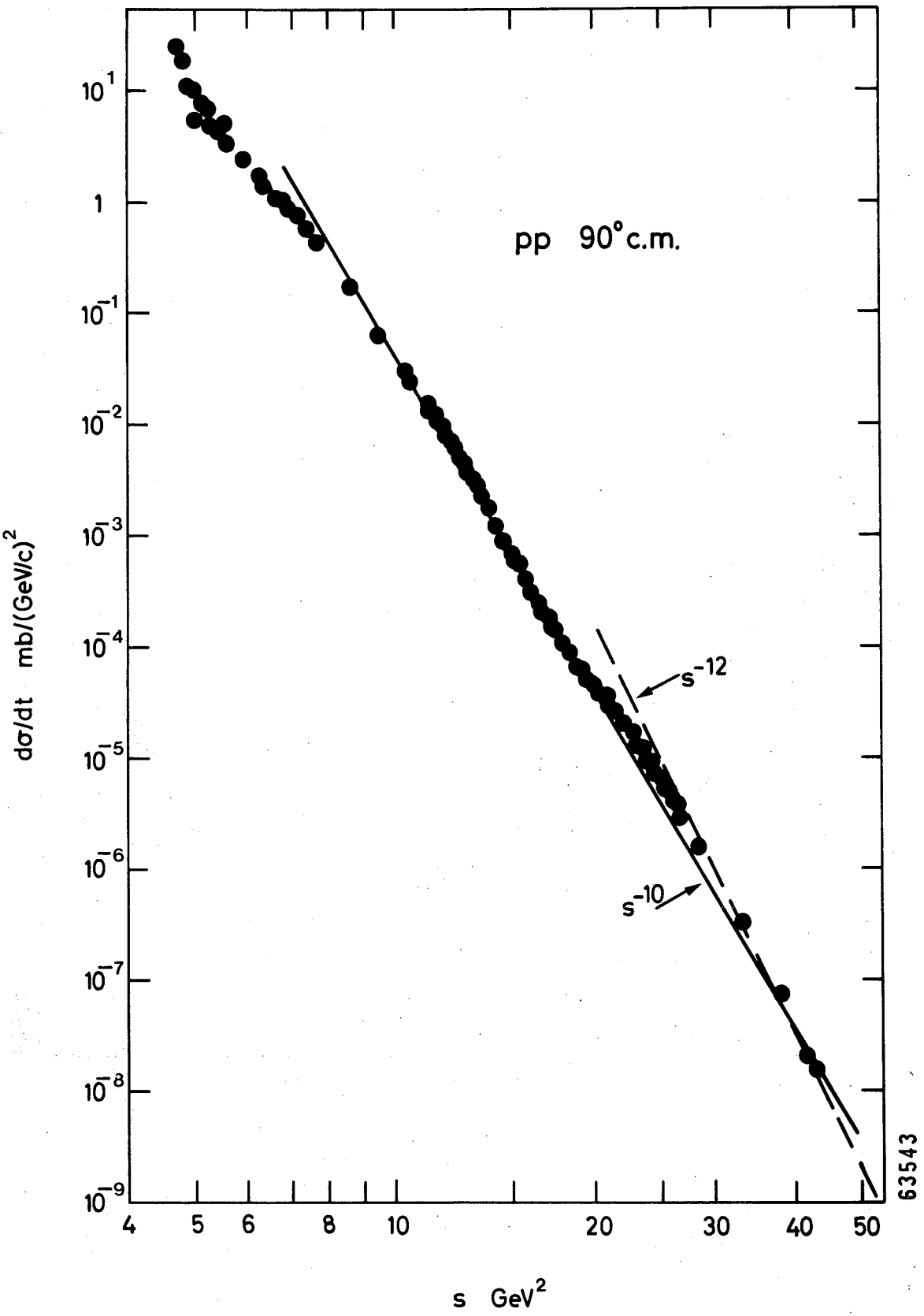
pp 90°c.m.
10^{1}
1
10^{-1}
10^{-2}
10^{-3}
10^{-4}
10^{-5}
10^{-6}
10^{-7}
10^{-8}
10^{-9}
s^{-12}
s^{-10}
4
5
6
8
10
20
30
40
50
$d\sigma/dt$ mb/(GeV/c)^2
s GeV^2
63543

Fig. 29

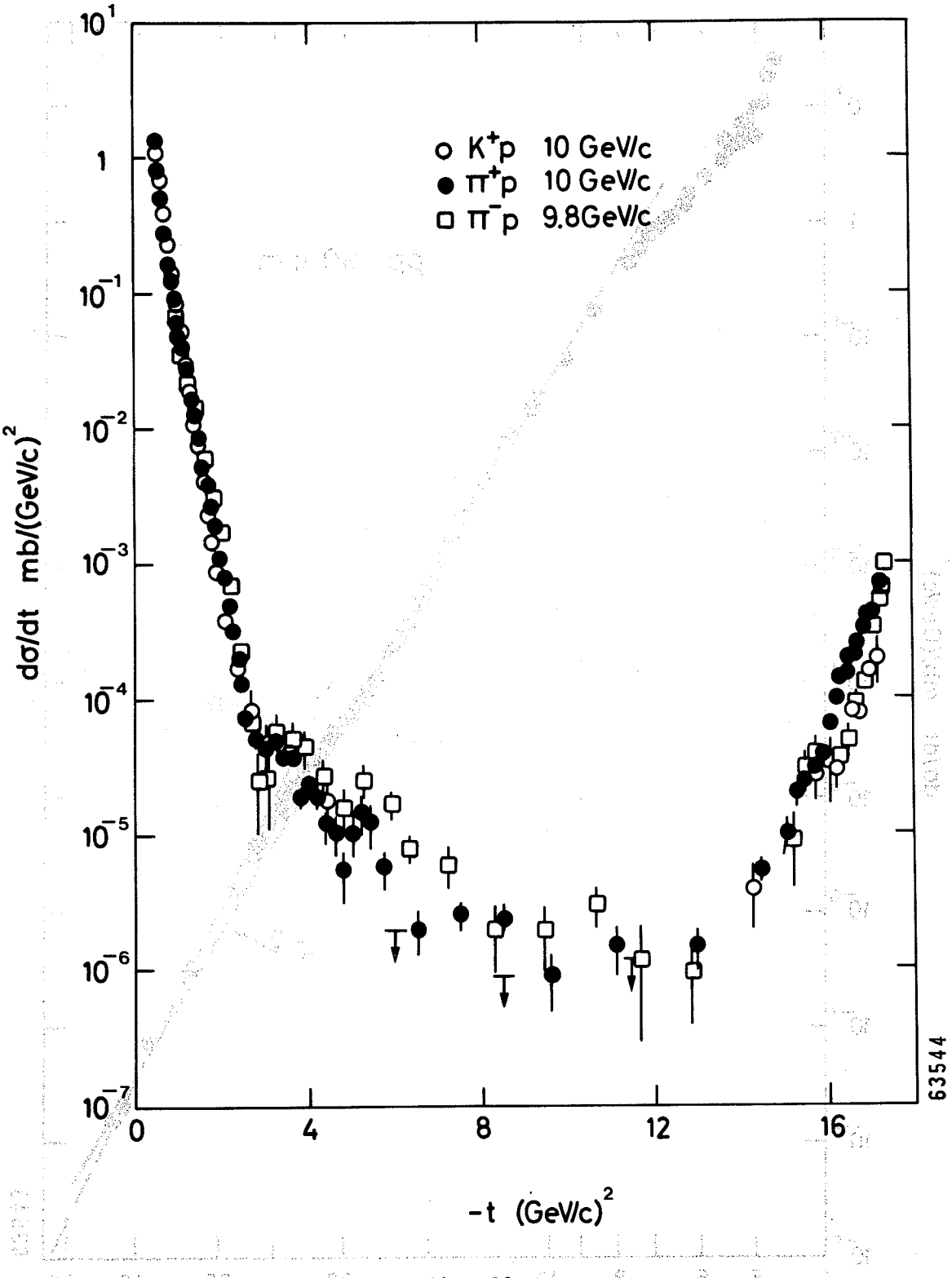

Fig. 30